ANL-HEP-PR-96-36

Measurement of the differences in the total cross section for antiparallel and parallel longitudinal spins and a measurement of parity nonconservation with incident polarized protons and antiprotons at 200 GeV/c

D.P. Grosnick, D.A. Hill, T. Kasprzyk, D. Lopiano, Y. Ohashi, * J. Sheppard, T. Shima,†
H. Spinka, R. Stanek, D.G. Underwood, and A. Yokosawa

Argonne National Laboratory, Argonne, Illinois 60439

J. Bystricky, P. Chaumette, J. Derégel, G. Durand, J. Fabre, F. Lehar, A. de Lesquen, and
L. van Rossum

DAPNIA, Centre d'Etudes Nucléaires de Saclay, F-91191 Gif-sur-Yvette, France

F.C. Luehring,‡ D.H. Miller, and P. Shanahan§

Physics Department, Northwestern University, Evanston, Illinois 60201

K.W. Krueger

Physics Department, Fort Hays State University, Hays, Kansas 67601

J.D. Cossairt and A.L. Read

Fermi National Accelerator Laboratory, Batavia, Illinois 60510

K. Iwatani

Faculty of Engineering, Hiroshima University, Higashi-Hiroshima 724, Japan

N.I. Belikov, A.A. Derevschikov, O.A. Grachov, Yu.A. Matulenko, A.P. Meschanin,
S.B. Nurushev, D.I. Patalakha, V.L. Rykov, V.L. Solovyanov, and A.N. Vasiliev

Institute of High Energy Physics, Serpukhov, Russian Federation

Work supported in part by the U.S. Department of Energy,
Division of High Energy Physics, Contract W-31-109-ENG-38.

N. Akchurin and Y. Onel

Department of Physics, University of Iowa, Iowa City, Iowa 52242

T. Maki

University of Occupational and Environmental Health, Kita-Kyushu 807, Japan

H. En'yo, H. Funahashi, Y. Goto, T. Iijima,** K. Imai, Y. Itow,†† S. Makino,‡‡ A. Masaike, K. Miyake, T. Nagamine,§§ N. Saito,*** and S. Yamashita†††

Department of Physics, Kyoto University, Kyoto 606-01, Japan

R. Takashima

Kyoto University of Education, Kyoto 612, Japan

F. Takeutchi

Kyoto-Sangyo University, Kyoto 612, Japan

K. Kuroda and A. Michalowicz

Laboratoire de Physique des Particules, BP909, 74017 Annecy-le-Vieux, France

N. Tanaka‡‡‡

Los Alamos National Laboratory, Los Alamos, New Mexico 87545

G. Salvato and A. Villari‡‡‡

Dipartimento di Fisica, University of Messina, I-98100, Messina, Italy

N. Tamura§§§

Department of Physics, Okayama University, Okayama 800, Japan

T. Yoshida

Osaka City University, Osaka 558, Japan

M.D. Corcoran, J. Cranshaw, F. Nessi-Tedaldi,[****] M. Nessi,[****] C. Nguyen,[††††]
J.B. Roberts, J. Skeens, and J.L. White [‡‡‡‡]

T.W. Bonner Nuclear Laboratory, Rice University, Houston, Texas 77251

A. Bravar,[§§§§] A. Penzo, and P. Schiavon

Dipartimento di Fisica, University of Trieste, I-34100, Trieste, Italy

G. Pauletta

University of Udine, 33100 Udine, Italy

(E581/704 Collaboration)

(May 3, 1996)

Abstract

The highest-energy measurement of $\Delta\sigma_L\,(pp)$ and the first ever measurement of $\Delta\sigma_L\,(\bar{p}p)$, the differences between proton-proton and antiproton-

---

*Present address: Institute of Physical and Chemical Research, Wako, Saitama 351-01, Japan.

†Present address: Kyoto Academy of International Culture, Katashirakawa, Sakyo-ku, Kyoto, Japan.

‡Present address: Indiana University, Bloomington, IN 47405.

§Present address: Fermi National Accelerator Laboratory, Batavia, IL 60510.

**Present address: National Laboratory for High Energy Physics, Tsukuba, Ibaraki 305, Japan.

††Present address: Institute for Cosmic Ray Research, University of Tokyo, Higashi-Mozumi, Kamioka-cho, Yoshiki-gun, Gifu 506-12, Japan.

‡‡Present address: Wakayama Medical College, Hironishi 651, Wakayama 649-63, Japan.

§§Present address: Department of Physics, Tohoku University, Aobaku, Sendai 980, Japan.

***Present address: Radiation Laboratory, RIKEN, Wako, Saitama 351-01, Japan.

†††Present address: International Center for Elementary Particle Physics (ICEPP), University of Tokyo, Hongo, Bunkyo-ku, Tokyo 113, Japan.

‡‡‡Deceased.

§§§Present address: Department of Physics, Niigata University, Niigata 950-21, Japan.

**** Present address: CERN, CH-1211 Geneva 23, Switzerland.

†††† Present address: University of Texas, Austin, TX 78712.

‡‡‡‡ Present address: American University, Washington, D.C. 20016.

§§§§ Present address: University of Mainz, D-55099, Mainz, Germany.

proton total cross sections for pure longitudinal spin states, are described. Data were taken using 200-GeV/c polarized beams incident on a polarized-proton target. The results are measured to be $\Delta\sigma_L\,(pp) = -42 \pm 48\,(\text{stat.}) \pm 53\,(\text{sys.})\,\mu\text{b}$ and $\Delta\sigma_L\,(\bar{p}p) = -256 \pm 124\,(\text{stat.}) \pm 109\,(\text{sys.})\,\mu\text{b}$. Many tests of systematic effects were investigated and are described, and a comparison to theoretical predictions is also given. Measurements of parity-nonconservation at 200 GeV/c in proton scattering and the first ever of antiproton scattering have also been derived from these data. The values are consistent with zero at the 10^{-5} level.

PACS number(s): 13.88.+e, 13.85.−t, 13.85.Lg, 11.30.Er

I. INTRODUCTION

New measurements of hadron-hadron scattering in pure, longitudinal spin states, $\Delta\sigma_L(pp)$ and $\Delta\sigma_L(\bar{p}p)$, have been performed at 200 GeV/c using polarized proton and antiproton beams and a polarized-proton target. The quantity, $\Delta\sigma_L = \sigma(\rightleftarrows) - \sigma(\rightrightarrows)$, is the difference of the total cross sections between spin states of the beam and target particles aligned antiparallel and parallel. In these measurements, the particle masses are small compared with the beam-particle energy.

Some previous experiments have indicated significant spin effects at high energies. Inclusive production of pions at 200 GeV/c has shown large asymmetries as a function of the Feynman variable, x_F [1]. Hyperons produced inclusively at 800 GeV/c have been observed to have large polarization values [2]. Elastic scattering of polarized protons have also shown significant spin effects [3]. Considering these measurements, and since the spin-dependent cross sections are almost completely unknown at high energies, it is possible that a difference in the total cross sections for longitudinal spin states may also be sizeable. The unpolarized, total cross section in p-p scattering increases by about a millibarn near 200 GeV/c [4] from the minimum in the cross section curve. This experiment investigates to what extent the helicity-changing amplitudes participate. Significant polarization effects may be expected in $\bar{p}$-p interactions at 200 GeV/c. In the annihilation of two spin-1/2 particles into vector intermediate states, such as a quark and an antiquark annihilating into vector gluons at energies where their masses can be neglected, the reaction rate for particles with the same helicities is suppressed relative to that with opposite helicities [5]. Therefore, the longitudinal spin-dependence of a process dominated by this annihilation could be large.

Nucleon-nucleon, or antinucleon-nucleon, elastic scattering can be described by a total of 16 possible amplitudes, 5 of which are independent by using the generalized Pauli principle and parity conservation in the strong interactions. One common representation of these nucleon-nucleon elastic amplitudes is the set of s-channel helicity amplitudes of Jacob and Wick [6]:

$$\begin{aligned}
\phi_1 &= \langle + + | + + \rangle \\
\phi_2 &= \langle + + | - - \rangle \\
\phi_3 &= \langle + - | + - \rangle \\
\phi_4 &= \langle + - | - + \rangle \\
\phi_5 &= \langle + + | + - \rangle \, ,
\end{aligned} \tag{1}$$

where $+$ and $-$ refer to the nucleon or antinucleon helicities in the c.m. frame. As a consequence of helicity conservation at $0°$, $\phi_4(0) = 0 = \phi_5(0)$.

Another representation [7] is the t-channel exchange amplitudes, N_0, N_1, N_2, U_0, and U_2, which have definite quantum numbers exchanged at asymptotic energies. These amplitudes are related to the previous representation by:

$$\begin{aligned}
N_0 &= \frac{1}{2}(\phi_1 + \phi_3) \\
N_1 &= \phi_5 \\
N_2 &= \frac{1}{2}(\phi_4 - \phi_2) \\
U_0 &= \frac{1}{2}(\phi_1 - \phi_3) \\
U_2 &= \frac{1}{2}(\phi_2 + \phi_4) \, .
\end{aligned} \tag{2}$$

The N amplitudes represent natural-parity exchange, and the U amplitudes unnatural-parity exchange. The subscripts correspond to the total s-channel helicity flip.

The generalized optical theorem allows the three nucleon-nucleon or antinucleon-nucleon total cross sections to be expressed in terms of the imaginary parts of the three nonzero forward amplitudes [8]:

$$\begin{aligned}
\sigma_{tot} &= \frac{1}{2}\left[\sigma(\rightleftarrows) + \sigma(\rightrightarrows)\right] \;=\; \frac{1}{2}\left[\sigma(\uparrow\downarrow) + \sigma(\uparrow\uparrow)\right] \\
&= \frac{2\pi}{k} \,\mathrm{Im}\, \left[\phi_1(0) + \phi_3(0)\right] \;=\; \frac{4\pi}{k} \,\mathrm{Im}\, N_0
\end{aligned}$$

$$\Delta\sigma_L = \sigma(\rightleftarrows) - \sigma(\rightrightarrows) \tag{3}$$

$$= \frac{4\pi}{k} \mathrm{Im}\,[\phi_1(0) - \phi_3(0)] \;=\; \frac{8\pi}{k} \mathrm{Im}\, U_0$$

$$\Delta\sigma_T = \sigma(\uparrow\downarrow) - \sigma(\uparrow\uparrow)$$

$$= -\frac{4\pi}{k} \mathrm{Im}\,[\phi_2(0)] \;=\; -\frac{8\pi}{k} \mathrm{Im}\, U_2\,,$$

where k is the c.m. momentum, $\sigma(\rightrightarrows)$ is the total cross section for parallel longitudinal spin states in the laboratory frame, $\sigma(\uparrow\downarrow)$ is the cross section for antiparallel transverse spin states, etc. Measurements of these three total cross sections for nucleon-nucleon interactions have been quite important for the determination of the elastic amplitudes at energies below about 3 GeV.

There have been many previous measurements of $\Delta\sigma_L\,(pp)$ that ranged from 200 MeV to 12 GeV, and they are shown in Fig. 1. The first measurements [9] were made at the Argonne ZGS with the proton beam momentum in the range, 1.0–3.6 GeV/c. The results indicated unexpected structure as a function of energy. Later measurements at the ZGS extended the beam momentum range to about 12 GeV/c [10]. Other $\Delta\sigma_L\,(pp)$ values were measured in experiments at energies between 300–800 MeV at LAMPF [11], 500–2800 MeV at SATURNE II [12], 200–500 MeV at TRIUMF [13], and 200–600 MeV at SIN [14]; all experiments used polarized-proton beams and targets. The concentration of data in the intermediate-energy range was to assist in the definition of the nucleon-nucleon amplitudes, and to understand the observed structure.

One explanation of the observed structure has been the resonance-like behavior in the p-p system and the possible existence of 6-quark states or dibaryons. A variety of QCD-motivated models [15–21] have predicted many such states in the intermediate-energy range. An alternate explanation has been the opening of inelastic channels, such as πd and especially $N\Delta$ [22,23], but this explanation has been challenged for several reasons [24–29]. However, similar structure has also been observed in isospin-0 nucleon-nucleon reactions, derived from np scattering experiments [30–34]. The πd and $N\Delta$ channels do not couple to isospin-0 nucleon-nucleon reactions, and the $\Delta\Delta$, NN^*, etc. channels occur at energies somewhat

above the observed structure. If mechanisms other than 6-quark states are responsible for the energy-dependent structure in the $\Delta\sigma_L$ (and $\Delta\sigma_T$) data, then some important ingredient must be missing or incorrect in the present models predicting these states.

At energies above a few GeV, there are fewer measurements and the evidence of structure is lacking. The trend of the data can be described by a power law at energies greater than about 4 GeV.

No previous measurements have been made of $\Delta\sigma_L(pp)$ at energies higher than 12 GeV, and no measurements have ever been made of $\Delta\sigma_L(\bar{p}p)$ at any energy. At high energies, the role of spin involving the hadron's constituents can be explored. Only two theoretical models exist to explain $\Delta\sigma_L(pp)$ at high energies, and no published theoretical prediction exists to describe $\Delta\sigma_L(\bar{p}p)$. Values of the parity nonconservation parameter, A_L, were derived from the data in this experiment by averaging over the target polarization. These data are compared to high-energy predictions.

A summary of the experimental setup, which describes the polarized beam, polarized target, detectors, and electronic logic, is presented in Sec. II. Section III describes the calculation of $\Delta\sigma_L$. The data analysis and results are presented in Sec. IV, along with a description of tests performed to understand the systematic errors. Section V includes a description and calculation of the parity-nonconserving quantity, A_L. A summary of the experiment and of the results is given in Sec. VI.

II. EXPERIMENTAL METHOD

A. Polarized beam

The 200-GeV/c polarized proton and antiproton beams were produced by the parity-nonconserving decays of the Λ and $\overline{\Lambda}$, respectively. No polarized source or polarized particle acceleration was used. In the polarized particle beam line, the protons and antiprotons were produced within a small phase space by the beam optics, and their spin directions mea-

sured and controlled by the beam-tagging and the spin-rotation magnet systems. Complete descriptions of the beam line and its properties are presented in Ref. [35].

The polarized proton and antiproton beams were produced when an 800-GeV/c unpolarized proton beam struck a Be target and produced Λ and $\overline{\Lambda}$ particles. As shown in Fig. 2, dipole sweeping magnets, located downstream of the production target, bent the unwanted charged-particle beam into a beam dump, while the neutral particles proceeded to a region where the Λ particles decayed. Remaining neutral particles continued to a neutral beam dump, as the charged particles from Λ and K^0 decays were bent around this dump region. The second bend in the beam line was located around the intermediate focus and was used in the momentum analysis of the beam particles. An adjustable vertical collimator, which was placed upstream of the intermediate focus, was used to vary the beam momentum bite, typically $\pm 9\%$, around the nominal beam momentum value of 200 GeV/c. The electronic beam-tagging system, which used 6 planes of scintillators, was situated at the intermediate focus to determine the momentum and polarization of a beam particle. Two Čerenkov counters were located in the beam to differentiate between protons and background pions. A set of spin-rotation magnets precessed the spins of the beam particles so that these spins were aligned longitudinally to the beam momentum before the particles struck the experimental polarized target, located at the final focus.

An average polarization direction of many protons can be measured by particle detectors, even though an individual proton's spin is not well defined. This average polarization direction in a given element of phase space is called the proton polarization direction.

1. Polarized beam production

Unpolarized protons were accelerated to 800 GeV/c in the Fermilab Tevatron and were extracted over a 20 s spill in a total acceleration cycle of about 1 min. During this measurement, typically 5×10^{12} protons per spill were incident on a beryllium production target, which had a width of 1.5 mm, height of 5.0 mm, and length of 30.0 cm. Among the many

particles produced in these collisions were unpolarized Λ and $\overline{\Lambda}$ hyperons.

The Λ particle then produced a proton in the parity-nonconserving decay, $\Lambda \rightarrow p + \pi^-$. Likewise, an antiproton was produced in the decay, $\overline{\Lambda} \rightarrow \overline{p} + \pi^+$. In the unpolarized Λ rest frame, the Λ decays isotropically with the spin direction of the proton aligned preferentially along the proton's momentum direction. The proton polarization from Λ decay had been measured previously as 64% [36]. The pion from the $\Lambda \rightarrow p + \pi^-$ decay was not tagged or used to determine the proton polarization.

In the laboratory reference frame, the trajectories of the protons from the Λ decays could be traced back to the plane of the production target. Protons with components of their momentum transverse to the Λ direction appeared to originate from a virtual source displaced from the actual Λ source. The transverse position at the virtual-source plane depended on the distance from the production target where the Λ decayed and on the angle at which the proton was emitted. The virtual source extended to about 1 cm on each side of the production target and was then imaged by the beam optics. Only those Λ ($\overline{\Lambda}$) decays that occurred between 9 and 30 m from the production target were accepted so that a more precise determination of the proton (antiproton) polarization could be made.

The beam-particle polarization was determined from a correlation between the position of the virtual source and the proton momentum direction, which was related to the proton polarization direction. At an intermediate focal point in the beam, each beam particle was tagged to determine its momentum and polarization. Only the horizontal component of the transverse proton or antiproton polarization was measured by the beam-tagging system. Using this method, both signs of the beam polarization could be used within the same beam spill.

2. Polarized beam transport

The primary purposes of the beam optics were to maintain the correlation between the polarization state and the horizontal position, and to introduce no net spin precession.

These were accomplished using a beam design that contained three focal points: the virtual source, the intermediate focus, and the final focus. The beam-tagging system was located at the intermediate focus, 160 m downstream of the primary production target, and the polarized experimental target at the final focus, 320 m downstream. Bends in the beam line were vertical only and were made by sets of four dipole magnets that produced no net momentum dispersion and no particle spin precession.

The requirements for a polarized beam were most easily satisfied by using the mirror-symmetric design of two sets of quadrupole-magnet doublets. The focal conditions were then applied to each half of this symmetrical system. Two conditions were imposed to satisfy the requirement of no net spin precession, and consequently, preserved the correlation between the polarization state and the virtual-source position: (1) point-to-point focusing and (2) parallel-to-parallel focusing. Two quadrupole doublets brought the beam to a focus at an intermediate focus, downstream of the production target, and two more doublets were used for the final focus, at the experimental target. In Ref. [35], the positions of the quadrupole doublets were given for a beam momentum of 185 GeV/c. In this experiment, the nominal beam momentum was 200 GeV/c, and consequently the distances between the quadrupole magnets in the doublets were increased by 0.61 m or 0.87 m, depending on the position of the doublet.

The bending and focusing operations of the beam were kept as completely separate as possible from each other. The bending dipole magnets came in sets of four, entirely contained between two quadrupole doublets. Any displacement or angular deflection due to a single bend in the beam is restored by three subsequent bends. Each set of four dipoles produced no net momentum dispersion or particle spin precession.

A global cancellation of the proton spin precession by the quadrupoles was required for maintaining the spin direction through the entire beam line, and this ensured that no depolarization of the beam occurred. A local cancellation of the spin precession within the set of four dipole magnets was also necessary to ensure no net spin precession.

The polarized-antiproton beam was made in a completely analogous manner as the

polarized-proton beam. The $\overline{p}$ beam polarization was found from the relation of the $\overline{p}$ momentum direction and the position at the virtual source in the production target plane. The only change to the beam line when using polarized antiprotons was to reverse the polarities of both dipole and quadrupole magnets.

The polarized beam spot at the experimental target was measured to be 1.3 cm (FWHM). This spot was the same size for both protons and antiprotons. The beam line was capable of providing an average beam intensity per spill of about 2.5×10^7 polarized protons, with an average beam polarization of 0.45. The production rate at 200 GeV/c for polarized antiprotons is down by a factor of 18 from polarized protons, due to the decrease in production of the $\overline{\Lambda}$. The pion contamination measured in the polarized-antiproton beam was about 83%.

Two threshold Čerenkov counters were used to separate protons and antiprotons from the pion contamination due to K^0 decays. These detectors were adjusted to reject the pions with maximum efficiency and veto only a few protons or antiprotons. Each detector measured a 13% pion contamination in the polarized-proton beam.

3. Spin-rotation magnets

A set of 12 spin-rotation magnets, called the "snake" magnets [37], were used to rotate the beam-particle polarization state from the S direction (normal and horizontal to the beam-particle momentum), which is the direction in which the spin component was actually tagged, to the L direction (along the particle momentum) or N direction (normal and vertical to the beam-particle momentum). The design [38] was such that no change in the particle trajectory was allowed through the snake magnets.

When rotating the beam-particle spin direction from S $\rightarrow$ L (horizontal to longitudinal), all 12 snake magnets were used. All 12 magnetic fields in the snake magnets must be reversed for the S $\rightarrow -$L configuration to rotate the particle spin by 180°. For some tests, the S $\rightarrow$ N spin rotation was used. In this case, only 8 of the 12 snake magnets were used, with only 4 magnetic fields reversed to change to a S $\rightarrow -$N spin rotation. The net spin rotation through

the snake magnets from the S $\rightarrow$ L states was opposite for protons and antiprotons. For S $\rightarrow$ N, the net spin rotation for protons and antiprotons was the same.

The beam-polarization direction was periodically reversed to minimize experimental systematic errors. The snake magnetic field directions were reversed every 12 spills, with 2 of these spills necessary to carry out the reversal process. Hall probes were installed within each magnet to monitor the magnitude of the field.

4. Polarized beam-tagging system

At the intermediate beam focal point, each beam particle was tagged electronically to determine its momentum and polarization. A total of six planes of scintillators detected the particle trajectory; three of these measured hits in the vertical direction to determine the momentum, and three measured hits in the horizontal to specify the polarization. Two of the three planes of scintillators measuring momentum were located before a bending magnet and the third after so that the angle of deflection, and the momentum, could be determined. Once the momentum of the particle was known, the location of the intermediate focus along the beam axis could be determined. The three planes of scintillators measuring trajectories in the horizontal direction were located at the nominal intermediate focus of the beam line, and 9.3 m before and after this location. The particle polarization was determined by interpolating the horizontal displacement at the momentum-dependent focal position, found by the scintillator planes, with respect to the given 200-GeV/c momentum trajectory.

Three beam scintillation counters formed the fast trigger for the beam-tagging system. A coincidence of all three counters indicated a particle passed through the intermediate focus, and then this signal enabled the rest of the beam-tagging electronics. Once a coincidence was made, no other coincidence was allowed for around 60 ns afterwards so that the scintillator-plane signals could be processed. Signals were encoded and processed in a manner similar to that described later in this section for the $\Delta\sigma_L$ experimental trigger. The momentum and polarization for a valid beam particle was measured within 250 ns. The electronic logic was

slightly modified from Ref. [35]. The encoded momentum values ranged from 8.7% less than the 200-GeV/c value to 8.7% greater. The encoded polarization values went from -0.75 to $+0.75$ in steps of 0.1. Particles were assigned a negative ($-$) polarization when their tagged values were between -0.35 and -0.55, a positive ($+$) polarization when the tagged values were between $+0.35$ and $+0.55$, and zero polarization when the tagged values were between -0.25 and $+0.25$. The distribution of tagged polarization values for the entire data sample with protons is shown in Fig. 3. The beam-tagging system worked in precisely the same manner for both proton and antiproton beams.

The beam-tagging system operated reliably and efficiently during the data-taking periods. Its operation was monitored in the same manner that will be described later using the sampling trigger. The use of many planes of scintillators provided beam diagnostics on-line, and information from the beam-tagging system was used extensively to properly tune the polarized beam.

5. Beam-polarization measurements

The beam-tagging system assigned a polarization value for each beam particle relative to a known trajectory. The validity of this system was verified by absolute measurements of the beam polarization using two polarimeters developed for high-energy polarized beams: the Primakoff-effect polarimeter and the Coulomb-nuclear interference (CNI) polarimeter. The two polarimeters used completely different reactions that result in an asymmetry in the scattering process to obtain the beam polarization.

The Primakoff-effect polarimeter [39] determined the proton-beam polarization by measuring the asymmetry in coherent Coulomb dissociation [40], in which an incident proton is converted to a p-π^0 system in the Coulomb field of a high-Z, nuclear target. This reaction, when produced at high energy, is related to the low-energy photoproduction of a π^0 from a proton. The beam polarization can then be determined from the low-energy data [41] and the measured asymmetry. The polarimeter consisted of a lead target to produce the p-π^0

system, a segmented lead-glass calorimeter that detected the 2 photons from the π^0 decay, and a magnetic spectrometer that detected the proton. The average beam polarization was measured to be $0.40 \pm 0.09\,(\text{stat.}) \pm 0.15(\text{sys.})$, compared to 0.45 given by the beam-tagging system.

The CNI polarimeter [42] determined the beam polarization by measuring the asymmetry in the interference region with a range of momentum transfer squared, $1 < -t < 30 \times 10^{-3}\,(\text{GeV}/c)^2$ for polarized proton-proton elastic scattering. The analyzing power for this process comes from the interference term between the nuclear non-flip amplitude and the electromagnetic spin-flip amplitude [43]. This process is almost independent of the beam energy. The polarimeter itself consisted of several scintillating targets that detected the recoil protons, and a magnetic spectrometer that determined the momentum of the scattered proton. The beam polarization was found to be (0.45 ± 0.17), compared to the tagged-beam polarization of 0.45.

Both polarimeters have demonstrated the polarization of the proton beam and verified the beam-tagging measurements. Polarimeter data using the polarized-antiproton beam were limited, and considering this, the results were similar to those of a polarized-proton beam. The relative systematic error on the absolute beam polarization was estimated to be $\pm 6\%$. The nominal beam momentum was 200 Gev/c and the relative systematic error was estimated to be $\pm 3\%$.

B. Polarized target

The polarized-proton target [44] used in this experiment was a frozen-spin type [45] that used the method of dynamic nuclear polarization [46] to align the target protons preferentially in a longitudinal direction along the beam axis. The target assembly, displayed in Fig. 4, consisted primarily of a ^{3}He-^{4}He dilution refrigerator, a superconducting solenoid, and a nuclear magnetic resonance (NMR) detection system. All target controls and monitors were remotely located from the target.

The polarized-target volume was cylindrical, with a 3-cm diameter and 20-cm length. It was filled with approximately 2-mm diameter beads of frozen 1-pentanol ($C_5H_{12}O$), containing 6 wt.% water, doped with the paramagnetic material [47], EHBA-Cr(V). Pentanol contains one polarizable, free proton for about six, unpolarizable, bound nucleons. The effective polarization dilution factor, including the liquid helium and target windows was 8.4. The beads were estimated to fill at least 98% of the entire target volume with a packing fraction of 0.63, and have a density of $0.62\,\mathrm{g/cm^3}$. The target constant, A, for free protons was $1040 \pm 38\,\mathrm{mb}$, where $A = (N_A\,\rho\,L)^{-1}$ and N_A is Avogadro's number, ρ is the free proton density, and L is the target length.

The superconducting solenoid had an overall length of 86 cm and a warm bore diameter of 9.4 cm. It used 1.5 l/hr of liquid helium, including transfers. The solenoid had a maximum field strength capacity of 6.5 T when powered at 185 A. For this experiment, the solenoid was operated at 2.5 T. The field uniformity in the target volume was better than $\Delta\,B/B = \pm 5 \times 10^{-5}$. In the frozen-spin mode, the center of the solenoid could be moved upstream 16 cm from the center of the target, with a magnetic field greater than 1.9 T remaining in the target volume. A portion of the target volume remains within the homogeneous magnetic field region while in the frozen-spin position. An unobstructed solid angle of 130 mrad with respect to the beam axis was formed at the exit of the target in this solenoid position.

The ^{3}He-^{4}He dilution refrigerator was a separate unit from the polarizing solenoid, and laid horizontally with a coaxial geometry that had a center channel so that the unobstructed beam could be incident on the target. The target container was attached to the end of a quick-load insertion for installing the target material while all parts of the refrigerator were cold and under a helium atmosphere. The circulating pumps had a displacement of $5500\,\mathrm{m^3/hr}$. The temperature achieved in the frozen-spin mode was about 60 mK with a 4 mmol/s flow of ^{3}He. Temperatures were measured by carbon resistors, calibrated against standard germanium resistors. In the polarizing mode, the ^{3}He flow was around 24 mmol/s. The entire target apparatus stood on a table that could be moved perpendicular to the beam direction and necessitated an articulated ^{3}He pump line. The liquid ^{4}He was supplied

through a flexible transfer line by a remote liquifier. A leak in the ^{3}He pump caused some difficulty during the data-taking period, and consequently the target-polarization direction was changed less frequently than desired. At frozen-spin temperatures of less than 80 mK, the proton spin relaxation time was greater than 50 days.

Microwave frequencies near 70 GHz were supplied by a carcinotron and provided the appropriate change in energy levels for enhancing the number of target protons in a particular spin state. Reversal of the target polarization was accomplished by a small change of microwave frequency.

The target polarization was measured using an NMR system [48] operating at 107 MHz. Signals were detected in three NMR coils and were processed using signal averaging. Each detector coil measured the target polarization at a different location of the target. One of the three NMR coils was located at the upstream end of the target, another at the downstream end, and the third in the middle. Because of an internal open circuit, the middle coil was inoperative during data accumulation. The NMR system was reasonably stable, measured to be better than 5%, throughout the entire data-taking period. No significant difference was seen in the NMR coils between the upstream and downstream target ends, and also in the target polarization values between polarizing and frozen-spin magnet configurations. The polarized-target data were transferred through CAMAC to the experimental computer. During frozen-spin mode, measurements of the target polarization were made once every several hours, with no movement of the polarizing solenoid.

The absolute target polarization was found by comparing the enhanced spin state signal with that of a signal produced when the target material was at thermal equilibrium near 1 K. The free protons were typically polarized to either $P_T = 0.77$ or $P_T = -0.80$, in approximately 3–4 hours. The mean decay rate of the polarization was $1.51 \pm 0.16\%$ per day while in frozen spin mode.

An off-line analysis [49] established the target calibration for the entire data-taking period. The estimated uncertainty (2σ estimate) on P_T was established at $\pm 6.5\%$. This value included contributions from the temperature and statistical uncertainties of the thermal

equilibrium NMR measurement, the NMR background, nonlinearity and residual drift, the spatial uniformity of the polarization, and errors due to interpolation and extrapolation. Most of these error contributions were symmetrical and uncorrelated.

A positive sign for P_T corresponded to a predominant occupation of the lower Zeeman state, or an enhancement of the spins of the target protons aligned parallel to the magnetic field of the target solenoid. Since this field pointed upstream in this experiment, positive values of P_T referred to the target spins aligned antiparallel to the incoming beam-particle momentum. The sign of the target polarization was reversed about once per day to reduce possible systematic effects related to the beam polarization reversal.

C. Detectors

1. Scintillator hodoscopes

A total of three scintillator hodoscope detectors were used to define the incoming beam-particle trajectory, and to determine the amount of interaction the beam particle encountered in the polarized target. Each hodoscope consisted of two planes of scintillators that measured the particle position in the horizontal (X) and vertical (Y) directions. These detectors are shown in Fig. 5.

The first detector had two of these hodoscope planes of scintillators, designated SNA1X and SNA1Y, located just upstream of the spin-rotation (snake) magnets and 23.79 m upstream of the experimental polarized target. Another two scintillator hodoscope planes, designated SNA2X and SNA2Y, were located 2.46 m upstream from the polarized target. These four hodoscopes measured the two spatial points that defined an incoming beam-particle trajectory. A third set of X and Y hodoscope planes, designated TRAX and TRAY and called the "transmission counter," was the first of two that were used to measure the amount of deflection in the beam-particle trajectory. This transmission counter was located 13.00 m downstream from the polarized target. The second transmission counter and asso-

ciated electronics were of a different design than the first, and are described in Sec. II C 4.

All 6 hodoscope planes were designed such that each scintillator overlapped its two neighbors by one-third (see Fig. 14 in Ref. [35]). Each third in X and Y was designated as a segment. Beam particles then interacted with either one or two scintillators as they proceeded through the hodoscope. This overlapping scintillator design allowed for more spatial segments and less encoding electronic logic, as well as leaving no gaps between scintillators.

The SNA1X and SNA1Y hodoscope planes consisted of 16 instrumented scintillators, which were 6-mm wide, 115-mm long, and 3-mm thick. The SNA1X plane had the 115-mm dimension in the vertical direction, so that the overlapping scintillator pattern was in the horizontal direction. The SNA1Y plane was rotated 90° with respect to SNA1X. Each segment was 2-mm wide, with an overall span of 6.6 cm. Each scintillator was attached to a 1.27-cm-diameter, ten-stage photomultiplier tube that produced a fast output signal. The SNA1X and SNA1Y scintillators were changed to a smaller 6-mm width from that given in Ref. [35] to improve the angular resolution of the incoming beam. The SNA2X and SNA2Y hodoscope planes also consisted of 16 scintillators of the same dimensions as the upstream snake hodoscopes, and with a 2-mm segment size. A total of 31 segments defined the beam-particle position in each plane of the snake hodoscopes.

The first transmission counter consisted of 28 scintillators per plane, again with an overlapping design with a 2-mm segment size. A total of 55 segments per plane measured the particle position, giving a total active area of $11 \times 11\,\mathrm{cm}^2$. This area was much larger than the 25.7-mm (FWHM) size of the beam at this point. Each scintillator was viewed by a single, 1.27-cm-diameter photomultiplier. The accuracy with which each of the scintillators was aligned with respect to each other within a hodoscope plane was less than 0.5 mm.

2. *Veto counters*

Two scintillator veto counters were added to the experiment so that the number of triggers from muon beam halo and from particles that would miss the polarized-target material would be reduced. The first veto counter, or muon veto counter, was located just downstream of the last snake magnet, and 4.80 m upstream of the polarized target. The muon veto counter was constructed from a large, single piece of scintillator, with a $40.6 \times 40.6\,\mathrm{cm}^2$ area, 1.3-cm thick, viewed on the left and right sides of the beam by two photomultiplier tubes. A single hole, 5.1 cm in diameter, allowed passage of beam particles, while beam halo particles were detected within the scintillator. These detected halo particles were then vetoed in the trigger electronics.

The second veto counter, or target veto counter, was located 1.85 m upstream of the polarized target. It consisted of four scintillators, in two sets of two scintillators, each 6.35-mm thick and each viewed by a single photomultiplier tube. Two scintillators with a 2.7-cm-diameter semicircular hole in each, abutted each other to cover a $15.2 \times 15.2\,\mathrm{cm}^2$ area perpendicular to the beam direction, and formed a left-right veto. Likewise, the other two scintillators formed an up-down veto with an identical hole arrangement. These scintillators detected stray particles that would not interact in the polarized target, and were again vetoed in the electronic logic.

3. *Experimental electronic logic*

A schematic diagram of the $\Delta\sigma_L$ experimental electronic logic is given in Fig. 6. The output of each scintillator in all the hodoscopes first went into an amplifier, after which the signal was split into an analog-to-digital converter (ADC) for pulse-height information and into a discriminator for trigger logic signals. An output from the discriminator went into a coincidence register and into programmable logic units (PLUs). A combination of two PLUs was sufficient to encode the hodoscope segment number from the overlapping

scintillators within a snake hodoscope plane. In the first transmission counter, the odd- and even-numbered scintillators for each X and Y plane were encoded separately in PLUs, which in turn were combined into an overall X and Y segment hit. The purpose of the odd and even arrangement was to provide a better estimate of the hodoscope efficiency.

The encoded hit segments from all of the snake (SNA) hodoscopes defined a straight-line trajectory for each incoming beam particle. In order to unambiguously define this trajectory, a single-segment hit was required in each of the four hodoscope planes. The trajectory could then be projected onto the plane of the transmission counter for each beam particle. This point defined an undeflected trajectory by an unscattered particle. A memory look-up unit (MLU) took the hit segment in X from the upstream and downstream snake PLUs and output the undeflected-trajectory segment position. An identical arrangement was used for a segment position in the vertical direction. Using both the segment position of the undeflected trajectory and the encoded hit segment from the transmission counter, a difference in the X and Y positions could be calculated that is proportional to the amount of scattering the beam particle has undergone. The output of the undeflected-X MLU is combined with the transmission-counter X hit segment in a separate MLU to determine a ΔX value. An identical arrangement is used to calculate the ΔY value.

The amount of scattering, given in terms of the momentum transfer squared for elastic scattering, t, was determined by another MLU that used the ΔX and ΔY outputs, as well as the nominal beam-particle momentum. The outputs of this MLU were then put into a series of scalers, divided into the seven different polarization values and one for the sum of the outputs. The assigned beam-polarization value for each particle, provided by the beam-tagging system, strobed the appropriate scaler for the given t-value signal. The scaler quantities produced the number of particles per beam-polarization state for a given scattered t bin, as well as the total number of particle triggers.

Accidental triggers were also scaled in a similar manner, but the strobe signal to the scalers was delayed by about 115 ns. The delay corresponded to approximately 6 pulses of the accelerator microstructure.

The trigger signal that enabled all of the hodoscope segment encoding logic was defined by several beam and target veto detector requirements, the proper beam-particle tagging, and the computer and beam enabled signals. The beam requirement consisted of an OR of all the scintillator signals from a snake hodoscope plane that was formed at the discriminator. The output level of this OR was set so that there was at least one, but no greater than two, scintillator hits within a given hodoscope plane. This requirement for each snake hodoscope plane enhanced the fraction of beam-particle trajectories that were uniquely determined. The veto detector requirement was such that no signal came from any one of the following: the two beam-line Čerenkov counters, the muon veto counter, and the four target veto counters. A value for the beam-particle momentum and polarization must be provided by the beam-tagging system.

In addition to these requirements, the $\Delta\sigma_L$ trigger was generated whenever there was a single hit in each of the planes of the snake scintillator hodoscopes, given by the encoding PLUs. A unique beam-particle trajectory with known momentum and polarization could be determined at the target for events with a $\Delta\sigma_L$ trigger. This trigger was also used to strobe the t-value scalers. Most of the trigger logic gates had outputs read by scalers for diagnostic purposes.

Several other quantities were scaled in the $\Delta\sigma_L$ measurement. Some of these include: the number of particles tagged for positive, negative, and zero beam polarization, the beam-tagging system hits and diagnostics, the transmission counter performance, and the numbers of particles assigned with undeflected and scattered distances in both X and Y directions.

All of the scalers were read by the computer and written to magnetic tape every two seconds during the 20-s beam spill, as well as a final read at the end of the spill, making a total of 11 reads during the course of an accelerator cycle. The scalers were cleared after the final read at the end of every spill. A total of 728 scalers were read via a serial CAMAC connection of 4 crates, which included one where the beam particles were tagged, located approximately 130 m upstream of the experimental target. A PDP-11/45 was used to acquire the data from CAMAC through a general purpose interface.

A trigger was installed that ran at approximately 10 Hz to sample the outputs of the encoding electronics and to fill on-line histograms so that the entire detector system could be checked to see if it was functioning properly. Data that were gathered during these sampling triggers included the ADCs, segment hit patterns from each hodoscope, and the PLU and MLU outputs from each hodoscope. This sampling trigger was an invaluable diagnostic tool of the experiment performance for both on- and off-line analyses.

Data acquired from the sampling triggers were sent through a high-speed link to a VAX workstation, where standard software was used to view the data. Histograms were filled to observe the polarized beam positions and trajectories, using the numerous planes of beam-line scintillator hodoscopes. Beam tuning was accomplished by adjusting the magnet currents to optimize the beam position after viewing the sampling trigger histograms. Crude performance checks of the scintillator hodoscopes were also monitored with the sampling trigger. Several times per day a complete check of the experimental trigger and encoding electronics was made by analyzing events in detail so that any abnormalities could be found and corrected on-line. Other monitors included several segmented-wire ion chambers located in the primary proton beam.

4. Second transmission counter and electronics

A second transmission counter was used in the $\Delta\sigma_L$ measurements to provide important cross checks for the experiment. This detector was also an essential triggering device for the CNI polarimeter [42] that was performed in the same beam line. This transmission counter consisted of scintillators that used a different design from those in the beam-tagging and snake-magnet regions. Specialized electronics [50] tested if more than one incoming particle was present and if a unique segment was hit in the X and Y directions.

The second transmission counter was situated in the beam line a distance of 46 m downstream of the polarized target. Five pairs of scintillation counters were used to define the X position of a particle track, and another five pairs the Y position. Two additional scintil-

lators, each with an area of $16 \times 16\,\mathrm{cm}^2$, were located in front of and behind the X and Y counters, and were used to trigger the transmission counter. The thickness of all scintillators was 3 mm.

This transmission counter consisted of two sets of five pairs of plastic scintillation counters, with each counter consisting of strips of scintillating material. Figure 7 depicts the array of scintillators in the second transmission counter. Each pair of counters subtended the same $16 \times 16\,\mathrm{cm}^2$ total area, but the total active area for each counter was one-half of this amount. The other counter within the pair, or the "inverse counter," subtended the half not covered by the first. The active regions of the five pairs of counters were distributed to define $2^5 = 32$ segments in a Gray Code pattern [50]. A position was then determined from the 32 horizontal and 32 vertical segments; each segment had a width of 5.0 mm.

The Gray Code design for this transmission counter was chosen because: (1) the number of photomultiplier tubes required to instrument it was relatively small (20 tubes for 2×32 segments), (2) the boundaries between the active and inverse regions of a counter pair never lined up with the boundaries of another pair, (3) any error due to "edge effects" in the counters with the narrowest strips never generated a segment assignment that was more than one segment offset from the true segment, (4) internal consistency checks allowed the rejection of certain events, such as multiple-track events, and (5) every particle was detected by the same number of counters. The comparison of scintillator hits from active and inverse patterns allowed cases to be recognized where the resulting pattern was not consistent with a single track, but due to oblique or multiple tracks, edge effects, random concidences with background particles, photomultiplier tube noise, or counter and electronics inefficiencies. Patterns of hits from active and inverse hits, and the different types of inconsistent patterns were all monitored throughout the experiment.

Similar electronics were used for both transmission counters. The undeflected X and Y segments at the second transmission counter were calculated in MLUs from hits in the SNA1 and SNA2 hodoscopes. The quantities, ΔX, ΔY, and t, were generated in the same manner as described previously. Many signals were scaled to monitor this system perfor-

mance (events scattered up, down, left, and right; good and bad encoding of signals from the scintillation counters; etc.) and to also calculate values for $\Delta\sigma_L\,(pp)$ and $\Delta\sigma_L\,(\overline{p}p)$. Accidental coincidences, obtained by delaying the transmission counter signals relative to the $\Delta\sigma_L$ trigger signal, were found to be negligibly small.

For the second transmission counter, the signal that strobed the t-value scalers included a requirement on the beam in addition to the $\Delta\sigma_L$ trigger signal described above. A small, 3-mm-thick scintillation counter centered on the nominal beam line upstream of the polarized target was used with the specialized electronics described in Ref. [50]. The goal was to eliminate events with two or more particles within ± 150 ns of the beam particle in order to reduce rate-dependent effects. This was accomplished with delayed coincidences and anticoincidences, along with a special circuit (*SBF* = *Signal Bon Faisceau*) with a threshold set on the integrated analog signal from the counter. Approximately 15% of the $\Delta\sigma_L$ triggers were rejected with this additional requirement, including some single particle events with large energy loss.

III. CALCULATION OF $\Delta\sigma_L$

The difference in total cross sections for a given solid angle i, can be calculated from the relations,

$$ln\,(R^+) = -\frac{1}{A}\,\sigma'_{Tot} - \frac{P_B\,P_T}{2\,A}\Delta\sigma_L$$

$$ln\,(R^-) = -\frac{1}{A}\,\sigma'_{Tot} + \frac{P_B\,P_T}{2\,A}\Delta\sigma_L$$

$$\Delta\sigma_{L,i} = -\frac{A}{P_B\,P_T}\ln\left(\frac{R_i^+}{R_i^-}\right) \approx -\frac{2\,A}{P_B\,P_T}\,\epsilon_i\,, \quad \text{where} \tag{4}$$

$$\epsilon_i = \frac{R_i^+ - R_i^-}{R_i^+ + R_i^-}\,, \text{ and} \tag{5}$$

$$R_i^\pm = \frac{N_i^\pm}{N_0^\pm}\,. \tag{6}$$

The target constant for free protons is A (see Sec. II B); P_B and P_T are the beam and target polarizations, respectively; $R_i^{\pm}$ is the ratio of the number of noninteracting beam particles, $N_i^{\pm}$, transmitted through the target in the i^{th} solid angle normalized to the number of incident particles, $N_0^{\pm}$, for (+) antiparallel and (−) parallel spin states. The total cross section for all of the nuclei in the beam line from the target to the transmission counter is σ'_{Tot}.

The statistical accuracy of a $\Delta\sigma_L$ experiment is proportional to the inverse of the square root of the total number of incident particles. Therefore, for about 10^{10} total particles measured, a statistical accuracy of $\sim 10^{-5}$ is obtained. This value corresponds to a $\sim 50\,\mu$b sensitivity in the $\Delta\sigma_L$ value.

This measurement of $\Delta\sigma_L$ was a transmission experiment where the difference in the number of noninteracting particles was counted in each spin state, parallel and antiparallel. This number was determined from a calculation of the square of the momentum transfer t for each particle,

$$t = -4\,|\overrightarrow{p}|^2 \sin^2\frac{\theta}{2} \;\approx\; -(p\,\theta)^2\,, \tag{7}$$

when the scattering is forward and the scattering angles are small. In the above equation, $\overrightarrow{p}$ is the beam-particle momentum and θ is the scattering angle. By projecting the incoming particle trajectory on to the plane of a finely-segmented detector grid, and comparing this value with the detector element that actually registers a "hit," a transverse distance can be calculated that is proportional to the scattering angle,

$$\theta \approx \frac{\Delta l}{d} = \frac{\sqrt{\Delta x^2 + \Delta y^2}}{d}\,, \tag{8}$$

where Δx and Δy are the distances between the projected segment that would be hit if there was no scattering, and the actual segment that was hit in the horizontal and vertical directions, respectively, and d is the distance from the target to the final detector. The t value is then calculated from

$$t = \frac{-p^2(\Delta x^2 + \Delta y^2)}{d^2}\,. \tag{9}$$

In this experiment, the value of p was nominally 200 GeV/c, the distance d was 13.00 m, and the ranges of Δx and Δy were 0–5 cm. The process of assigning a t bin to a particle scatter is depicted in Fig. 8. This calculation was performed on-line electronically in about 275 ns, when the signal originated from the snake hodoscope discriminator to the calculated value of t. Since large numbers of particles were needed to measure very small asymmetries, an offline reconstruction of each scattering event would have required enormous amounts of beam and computer time. Thus, the scaler experiment devised here can reach the desired sensitivity in a reasonable amount of time, with the disadvantage of having no second chance at reconstructing individual events in the data.

A total of 12 "t bins" were defined in the electronic trigger for the first transmission counter. The first four t bins had a width of 0.0052 $(\mathrm{GeV}/c)^2$ each, while t-bins 5–11 had a width of 0.0104 $(\mathrm{GeV}/c)^2$ each. Each t bin described an annulus on the face of the transmission counter. The twelfth t bin scaled the number of particles detected in the transmission counter, but were outside the range of the first 11 t bins. All those triggers that registered no or multiple hits in the transmission counter were also recorded. A log plot of the number of particles that were detected by the transmission counter as a function of the square of the four-momentum transfer, $-t$, is shown in Fig. 9 for all of the proton data. As indicated by this plot, most of the particle hits were located in the first t bin, corresponding to a large number of transmitted particles and to only a small fraction of those that were scattered at small angles. Most of the rest of the hits in the other t bins indicated particles that were scattered from the target. Also shown in Fig. 9 are dots representing the corrected numbers of hits per t bin. Since the transmission counter segments formed a 2-mm grid, and the t bins described annuli, there was a mismatch in the assignment of particles detected in a given transmission counter segment to the proper t bin. A Monte Carlo simulation was written to make this geometrical correction. The dashed line in Fig. 9 is a fit of the function, $\alpha \exp(\beta t + \gamma t^2) + \delta$, which was used by previous experiments in p-p and $\bar{p}$-p scattering [51], to the corrected data.

The second transmission counter electronics used eight t bins. The first t bin extended

to $-t = 0.002\,(\mathrm{GeV}/c)^2$, and the next six had a width of $0.005\,(\mathrm{GeV}/c)^2$, so that t-bin 7 had events with $-t \leq 0.032\,(\mathrm{GeV}/c)^2$. The eighth t bin included those events in the transmission counter that were outside the first seven t bins.

Since the total number of transmission counter hits in t-bin 1 was a combination of both transmitted and scattered (background) events, the transmission asymmetry could be written,

$$\epsilon \approx \frac{N_1^+ - B^+ - N_1^- + B^-}{N_1^+ - B^+ + N_1^- - B^-}$$
$$\approx \left[\left(\frac{N_1^+ - N_1^-}{N_1^+ + N_1^-}\right) - \left(\frac{B^+ - B^-}{B^+ + B^-}\right)\left(\frac{B^+ + B^-}{N_1^+ + N_1^-}\right)\right]\left[1 + \left(\frac{B^+ + B^-}{N_1^+ + N_1^-}\right)\right], \qquad (10)$$

where $N_1^\pm$ is the total number of hits in t-bin 1 for spin states that are $(+)$ antiparallel and $(-)$ parallel, $B^\pm$ is the number of background hits within t-bin 1 for antiparallel and parallel states, and $N_1^\pm = T^\pm + B^\pm$, where $T^\pm$ is the number of noninteracting particles detected by the transmission counter. The background is assumed to be small for this approximation. The term in Eq. (10) involving only N_1 is simply the asymmetry in the number of particles detected within t-bin 1 and named ϵ_1. Likewise, the term containing only B values is the asymmetry in the number of background particles and named ϵ_B. The quantity, $B^+ + B^-$, is the total amount of background particles, B, and $N_1^+ + N_1^-$ is the total number of particles detected within t-bin 1, N. Equation (10) can be rewritten to calculate the transmission asymmetry as

$$\epsilon \approx \left(1 + \frac{B}{N}\right)\epsilon_1 - \frac{B}{N}\epsilon_B\,. \qquad (11)$$

The value B/N is small, so the contribution of the background within t-bin 1 is small, as indicated in Fig. 9. This background consists mostly of small-angle scatters that are found in t-bin 1. The background contributes about 3% to the total number of particles within t-bin 1, and the number of transmitted particles is then about 97%. In Eq. (11), the contribution by ϵ_B to the transmission asymmetry ϵ is also small, so the major contribution to ϵ comes from the asymmetry in the total number of particles detected in t-bin 1, ϵ_1.

The method chosen to find the background asymmetry, ϵ_B, calculated the individual asymmetries for each t-bin i, ϵ_i. A straight-line fit was made through the ϵ_i data as a function of $-t$, excluding t-bins 1 and 2 because they contained some fraction of the number of transmitted particles. An extrapolation of the data along this line was made to $t = 0$, where the value of the asymmetry at this point was assigned to the value of ϵ_B. A plot of the asymmetries ϵ_i as a function of $-t$ is shown in Fig. 10 for the entire sample of protons with beam polarization values of 0.35–0.55. A straight-line fit to the data is also shown. An advantage in using this method is that the individual t-bin acceptances do not need to be known, and nonuniformities cancel when calculating the asymmetry.

Two other methods were investigated that could have determined the value for ϵ_B. The first used the function, $\alpha \exp(\beta t + \gamma t^2) + \delta$, to fit the corrected data points, as shown in Fig. 9. From this fit, the number of background hits was subtracted from the total number of hits within t-bin 1 so that the number of transmitted particles could be determined. An asymmetry was then calculated from the transmitted numbers for parallel and antiparallel spin states. The cumulative error on the asymmetry was very large due to the sensitivity of the background fit to the data. This method was also very dependent on the individual t-bin acceptances.

The second method again calculated individual asymmetries for each t bin, but did not fit a t dependence to the data. It instead took a weighted average of the asymmetry values for t-bins 3–11, and used this as the value for ϵ_B. The values obtained with this method were very similar to the chosen method.

A completely different analysis, described in Sec. IV B, was used for a variety of tests and another calculation of $\Delta\sigma_L$. This "global-fit" method considered all single hits within the transmission counters as originating from noninteracting, transmitted beam particles. It assumed that backgrounds from elastic scattering and inelastic reactions were negligible (B/N$\approx$ 0), and that asymmetries were constant as a function of t (see Fig. 10). Different cuts on the scaler data were also applied using this method compared to the final analysis. Yet again, the results from this analysis were very similar to the final method adopted.

Three different quantities were reversed in this experiment to reduce and cancel systematic errors. They were: (1) the direction of rotation of the beam-particle spin to + and − longitudinal spin states [snake state], (2) the + and − target polarization directions [target state], and (3) the tagged + and − beam-polarization directions [pol state]. A total of 8 unique sums are then defined according to the state of each of the three conditions above, and 4 of these 8 sums correspond to the parallel spin state, R_i^-, and 4 correspond to the antiparallel spin state, R_i^+. These 8 unique sums correspond to the spin states of the beam and target particles, shown in Fig. 11, by varying the three states described above. The values of $N_i^\pm$, $N_0^\pm$, and $R_i^\pm$ correspond to the parallel and antiparallel spin sums displayed in Fig. 11. For $\Delta\sigma_L$, the states (a)–(d) in Fig. 11 correspond to the parallel spin sum.

IV. DATA ANALYSIS AND RESULTS

A. Data from the first transmission counter

In order for a beam spill to be included in the data sample, it had to pass several hardware requirements for the $\Delta\sigma_L$ trigger, as well as some additional software requirements. The hardware requirements have been presented in a previous section. A beam particle had to have both a valid momentum and polarization value from the beam-tagging system. A single hit in each of the planes of the snake scintillator hodoscopes was also required to define a unique particle trajectory before the polarized target. In addition, no particles should have been detected by the veto counters. An event passing these requirements was considered to have a valid $\Delta\sigma_L$ trigger.

The software data requirements were implemented for each spill of data. The scaler values were not allowed to decrease during the several reads of the spill, unless the scaler limit had been exceeded and rolled over to a much lower value. The scalers recording events on the electronic logic gates in the trigger were required to show the proper decreasing progression of values as more hardware requirements were implemented. The spill was rejected and

removed from further analysis if this requirement did not hold for the beam-tagging logic and the $\Delta\sigma_L$ trigger logic. The other software requirements examined the t-bin values: (1) the number of particles within each t bin had to be less than the total number of triggers, (2) the sum of all the t-bin counts had to be equal to the total number of $\Delta\sigma_L$ triggers to within 1%, and (3) the transmission ratio of counts in t-bin 1 to total triggers had to be greater than 0.6. The first two t-bin requirements simply verified that the t-bin scaler numbers were reasonable, and the third checked that the transmission had not changed drastically.

Data were collected in alternating periods of + and − target polarizations, with interspersed use of polarized proton and antiproton beams. The total number of polarized protons tagged during the experiment was 1.28×10^{11}, which averaged to 6.2×10^6 polarized protons per spill. The total number of $\Delta\sigma_L$ triggers was 3.7×10^{10} with an average live time of 88%. Almost all of the dead time was due to the sampling trigger. The fraction of tagged-beam protons that satisfied the hardware requirement was 29.3%. The number of proton beam spills that survived the software requirements was 98%.

The total number of polarized antiprotons tagged for the experiment was 9.29×10^{10}, with an average of 4.2×10^6 per spill. The total number of $\Delta\sigma_L$ triggers was 6.3×10^9, with the same amount of live time as that for protons. The fraction of tagged-beam antiprotons that satisfied the hardware trigger was 6.8%. This difference in the number of triggers between protons and antiprotons was due to the factor of about 5 in the ratio of background pions to antiprotons in the beam. The number of spills that survived the software requirements was also about 98%.

The average magnitudes of the beam and target polarizations taken during the experiment were also determined. The average beam-polarization magnitude for values between 0.35–0.55 was found to be 0.4573 for protons and 0.4575 for antiprotons. The average tagged zero beam polarizations were 0.0013 for protons and 0.0007 for antiprotons. The average magnitudes of the target polarizations were 0.73 for the proton beam data and 0.78 for the antiproton beam data.

The number of accidental hits in the transmission counter was monitored during the

experiment. The rate of accidentals was about 1% of the total number of hits detected. There were some hardware problems in obtaining these numbers during the entire data sample, and also some difficulty in properly normalizing the measured accidentals. Because of this, the accidental subtraction was not used in the analysis. A check of the results using a portion of the data corrected and uncorrected for accidentals showed no difference in the asymmetry within statistics.

A large effort was made to calculate the efficiencies of the detector elements within the transmission counter. Due to the overlapping scintillator design, the efficiency calculation was complex. However, not all of the information to perform this calculation was available at all times during the experiment, and so the absolute efficiencies could not be determined. This correction to the number of hits was not included in the analysis. The relative efficiencies could be monitored from the distributions of hits within the detectors, and no large variations were observed during the data-taking period.

The values of the asymmetries, ϵ_1, ϵ_B, and ϵ, defined in Eq. (11), are displayed in Table I for the entire sample of proton and antiproton data using beam-polarization absolute values between 0.35–0.55. Also shown are the uncorrected, calculated values of $\Delta\sigma_L(pp)$ and $\Delta\sigma_L(\bar{p}p)$, using Eq. (4) and the values of ϵ calculated from Eq. (11), and the average magnitudes of the beam and target polarizations. The errors shown are statistical only, and all statistical errors were calculated using a binomial distribution. All the data values in Table I are consistent with zero. An asymmetry was calculated using data with no or multiple hits in the transmission counter, and was also found to be consistent with zero for both protons and antiprotons. Additional corrections to the data listed in Table I are described in Sec. IV E.

B. Data from the second transmission counter

An alternate analysis, the global-fit method, was used with data from both transmission counters. This method used 20 measured transmission rates expressed in terms of linear

combinations of 2 or 3 parameters: (1) the spin-averaged total cross section σ'_{Tot}, (2) the $\Delta\sigma_L$ value, and (3) the parity-nonconserving asymmetry A_L between + helicity and − helicity beam or target particles,

$$\ln R_j = -\frac{1}{A}\sigma'_{Tot} \pm \frac{P_{B_j} P_{T_j}}{2A}\Delta\sigma_L + ([\pm P_{B_j} \pm f P_{T_j}] A_L), \tag{12}$$

where f is the dilution factor for polarized protons compared to the total nucleons in the target. The 20 transmission rates (R_j) consisted of the 8 from the conditions shown in Fig. 11 with tagged-beam polarization magnitudes between 0.35 – 0.55, another 8 with the same conditions but for polarization magnitudes 0.25 – 0.35, and the 4 rates corresponding to combinations of the two target states and the two snake states with beam-polarization magnitudes between 0.0 – 0.25. Each rate corresponded to the sum of counts from the first two or more t bins, and there was no subtraction of background from scattering events, assuming the background was negligible. A fit was then made of the two or three parameters to the logarithm of the 20 transmission rates using a χ^2 minimization procedure. The weights of the 20 terms were adjusted to correspond to equal integrated beam intensity for + and − target polarizations, for beam polarizations tagged + and −, and for the two snake states. This procedure cancels one class of possible systematic errors as described below. A comparison of the $\Delta\sigma_L$ values using data from the two transmission counters and calculated with the two-parameter ($\sigma'_{Tot}, \Delta\sigma_L$), global-fit method was made with the results shown in Table II. It can be seen that the results in Tables I and II, using different detectors, electronics, and analysis methods, agree within 1.5 standard deviations. Most of the data were collected simultaneously with the two transmission counters, although there were periods when only one detector was operational. Hence, the two values in Table II are not independent. Since the exact degree of correlation between the data from the two transmission counters was not determined, these measurements have not been combined and the data from the first transmission counter, after correction, are quoted as the final results. Also, the data analyzed for the first transmission counter in the two tables had both slightly different data samples and requirements on the data.

The systematic errors in Table II were estimated by using a variety of different weights for the 20 transmission rate terms in the χ^2 minimization procedure. These included weights corresponding to the measured integrated beam intensity, so that the integrated beam intensity would be equal for the two target states or for the two beam polarization and two snake states, and the weights used for the data in Table II, as given above. The data fits were also performed for different sums of t-bin counts as well as the different weights. The estimated systematic errors were found from the variation of the parameters. The errors for $\Delta\sigma_L$ are comparable to the statistical uncertainties.

Some tests of the data were performed with the global-fit method. During one test, the ratio of the positive and negative target polarizations was varied from the nominal value by up to 15%. The effect on the $\Delta\sigma_L$ value from this variation was less than one-half of a standard deviation. Variations in the target polarization ratio were not expected to be this large, so the actual effect on $\Delta\sigma_L$ will also be smaller. Another test artificially varied the amount of beam absorption in the target by up to 8% during one snake state; the absorption was assumed to be the same for both target states and both beam polarization states. The result on $\Delta\sigma_L$ was less than one-half of a standard deviation. This difference in transmission during a given snake state was expected to be very small compared to 8%. Finally, the value of σ'_{Tot} derived from the global-fit analysis was close to the anticipated result, taking into account all the material in the target and the beam between the SNA2 hodoscope and the transmission counters. This value was usually very stable with time.

However, significant differences in the calculated parameters, especially A_L, were observed for subsets of the data when the transmission rate was different for the two target polarization states. Such differences occurred for the results from the second transmission counter when a helium gas bag, located between the two transmission counters, became deflated on several occasions. In principle, such experimental incidents should not affect the calculated $\Delta\sigma_L$ value if: (1) the fractional change in the transmission rate was the same for the two snake and the two beam polarization states, (2) the magnitude of the beam polarization for the two polarization states was the same, (3) the two target polarizations had

the same size, and (4) the integrated beam intensity was the same for all 8 conditions shown in Fig. 11. The adjustment of the weights in the χ^2 minimization procedure compensated for the last condition, and the beam-polarization magnitudes for particles tagged + and − were very nearly equal. However, the two target polarizations often differed by $\sim 4\%$, and it could not be guaranteed that the gas bags deflated in such a manner as to cause equal fractional changes to beam transmission for the two beam polarization states. Thus the data from the second transmission counter were not used for the determination of A_L.

Furthermore, there was a class of systematic effects that affected the beam transmission from one condition in Fig. 11 differently from the other 7 conditions; this situation could produce errors in both $\Delta\sigma_L$ and A_L. The global-fit method with Eq. (12) would have required modifications in order to search for such systematic effects. Instead, the background subtraction method presented in Secs. III and IV A was chosen to search and correct for additional systematic effects, as described in the following sections. This also has the advantage of minimizing certain types of systematic errors that could influence the determination of A_L, but not $\Delta\sigma_L$.

C. False asymmetries

As described previously, 8 unique sums are defined corresponding to the parallel (R_i^-) and antiparallel (R_i^+) spin states of the beam and target particles. By rearranging the 8 sums into different combinations of "parallel" and "antiparallel" states, a total of 35 independent combinations can be made. Each combination contains 4 parallel and 4 antiparallel spin sums, and combinations that are only transpositions in the sign are excluded. It is interesting to note that of these 35 combinations, only 4 are well-balanced in each of the three quantities (snake state, target state, and pol state), having two of each type of the three quantities in both the antiparallel and parallel states. Included in these 4 special combinations, are $\Delta\sigma_L$ and a sum over the polarized target states to give an effective measurement of parity. The other two special combinations should give an asymmetry value of zero, since adding

together pairs of variables produces an effective unpolarized beam and an unpolarized target.

One of these other two special combinations sums over the two beam-polarization states to give an effective zero beam polarization, or unpolarized beam, and forms a "fake zero" asymmetry, ϵ_F. In Fig. 11, the states (a), (b), (g), and (h) correspond to the "parallel" spin sum of ϵ_F. The other one of these special combinations sums over the two snake rotations to give an effective unpolarized beam and target, and forms a "fake rotation" asymmetry, ϵ_R. The states (b), (d), (e), and (g) in Fig. 11 correspond to the "parallel" sum of the ϵ_R asymmetry.

There are three other combinations of these 35 that warrant further scrutiny. Each of these three combinations contains only one state of the snake, target, and pol states in the "parallel" and "antiparallel" sums. Thus an asymmetry is formed that indicates how well the two reversible states cancel. The combination that contains 4 sums of one of the snake states gives a "fake snake" asymmetry, the one combination that contains 4 sums of one of the beam-polarization states gives a "fake beam pol" asymmetry, and the one combination that contains 4 sums of one of the polarized target states gives a "fake target" asymmetry. The other 28 independent combinations do not correspond to a physical meaning related to the experiment.

Of the total 8 possible sums in the asymmetry calculation as shown in Fig. 11, only 4 sums would be used if one of the three states (snake, target, or pol), was held constant. For example, if only one of the target polarization states was used, such as the + target state, contributions to the asymmetry would come from states (a) and (d) in Fig. 11 for the parallel sum, and from states (f) and (g) for the antiparallel sum. By holding each one of the three states constant, an estimate of how well the other two states cancel could be made, as well as the contribution from each state. The results of this analysis, giving the appropriate values for the transmission asymmetry ϵ and $\Delta\sigma_L$, are given in Table III for protons and antiprotons. The results show how well the quantities cancel, even though there are nonzero values when one of the states is fixed.

Several other false asymmetries were calculated to understand systematic effects and

provide information on the measurement. The beam particles that were tagged with zero (-0.25 to $+0.25$) polarization could also be used to calculate a "pol zero" asymmetry, ϵ_0. Of the 3 possible quantities that could change state, only the target and the snake states could be reversed to reduce systematic results for the pol zero asymmetry. The calculated value of the pol zero asymmetries are given in Table IV for protons and antiprotons.

Another quantity that was found to measure an effective zero beam polarization is a "fake zero" asymmetry, ϵ_F, as described previously. The number of beam particles tagged as "+" were added to those tagged as "−" to produce the number of particles with a fake zero polarization. An asymmetry was then calculated using these numbers and is also shown in Table IV for protons and antiprotons. An advantage of using the fake zero asymmetries is that it uses all 8 combinations of the 3 states shown in Fig. 11, while the pol zero asymmetry uses only 4 combinations, and with a completely different set of tagged beam particles. The calculated ϵ_0 and ϵ_F asymmetries are the same sign and magnitude, within statistics, of each other. The nonzero value may be due to a small misalignment of the transmission counter from the actual origin in X and Y from the assumed origin. Other evidence for a misalignment comes from the values calculated when holding one of the three states constant. The pol zero and fake zero asymmetries have the same magnitude and sign for the two polarized target states and the two beam polarization states. This indicates a constant offset explainable by a detector misalignment. This misalignment could also cause the wrong assignment of a t value for the scattered event in a given beam polarization state.

Two other asymmetries were formed and studied for possible effects: the "pairwise spill" asymmetry and the "snake off" asymmetry. By adding the number of particles in each t bin for every other spill, and calculating the asymmetry, ϵ_W, a measure of the change in experimental conditions on the time scale of a spill could be studied. The pairwise spill asymmetry is given in Table IV for protons and antiprotons; both values are consistent with no effect. The "snake off" asymmetry used particles and conditions during the one spill of 12 in the snake magnet reversal cycle when there was no current in the snake magnets, as indicated by the Hall probe values. This asymmetry was found to be unreliable due to

changing beam-motion conditions when reversing snake-magnet polarities.

D. Studies for the systematic error estimate

Many different studies were made of effects that could influence the data. Some of these studies included effects, such as the beam transmission, beam motion, and target density, on the three reversible states. Others included detector alignment, intensity, and a left-right asymmetry analysis. These studies were mostly performed with data from the first transmission counter, and similar results were observed with the second transmission counter.

1. Beam motion effects correlated with the snake state

One such study investigated the effects of changing the snake state, that is, by changing the direction of rotation of the beam-particle spin by the snake magnets to the longitudinal spin states. By forming left/right and up/down ratios from the number of particles measured in several detectors, the amount of beam motion correlated with the snake state could be observed. The veto scintillation counters and the scintillator hodoscopes, when viewed in this manner, all showed a periodic structure of 24 spills in the left/right ratio for both proton and antiproton data. This periodic structure corresponded directly to the reversal of snake states. Less structure was observed in the up/down ratio. The horizontal beam motion originated upstream of the snake magnets and downstream of the beam-tagging area. Even though the cause was never verified, the motion was probably due to a small vernier magnet, located between the two Čerenkov counters and not shown in Fig. 2, whose power supply was located near those of the snake magnets. The large currents used in the snake magnets influenced the power supply of the vernier magnet, as found by a linear relationship between the size of the effect and the snake magnet current. A check of this was performed to see if the difference in the vernier magnet current between the two snake states affected the asymmetry and the beam position. An approximately linear relationship was found between

the $\Delta\sigma_L$ asymmetry and the difference in vernier magnet current. A linear relationship was also observed with the pol zero asymmetry and the difference in current. This correlation caused no difficulties with the data as long as the snake magnet current remained constant.

The magnitude of this beam motion could be found from the centroids of the distribution of particles detected in the transmission counter. The difference in centroids between one snake state and the other showed a horizontal shift of (0.56 ± 0.07) mm for protons and (-0.51 ± 0.16) mm for antiprotons. Note that the shifts in the peak positions are opposite for protons and antiprotons, which also indicated that a bending magnet could be involved. The beam motion that was observed in this experiment was measured using data from the L-type snake configuration instead of the N-type configuration reported in Ref. [35]. The overall effect that this beam motion had on the transmission asymmetry was minimized because there were approximately equal numbers of spills with the snake magnets in each state, and also because the spin direction of the protons in the polarized target was reversed several times.

2. Beam transmission correlated with position

Another study showed that there was a difference in the beam-particle transmission as a function of the tagged-beam polarization state for both protons and antiprotons. The tagged + beam-polarization state always had a slightly larger transmission than for the − beam-polarization state. For example, in t-bin 1 the difference in transmission was 0.25% for protons and 0.29% for antiprotons. A plot of the beam-particle transmission as a function of beam polarization is shown in Fig. 12. Since the + and − beam-polarization states are physically located on different sides of the beam spot, it was conceivable that one part of the beam traversed a different part of the target or other material containing a different density than the other part. Such a different density in the target could be caused by the finite sizes of the beads or the nonparallel ends of the target volume. Another possible explanation was that a translation in the transmission counter caused a wrong assignment of the t bin for

the scattered particle. The number of particles assigned to t-bin 1 for one beam-polarization state could then be changed and cause a difference in the amount of beam transmission.

The effect of a translation in the position of the transmission counter on the data was investigated during a period when the transmission counter was shifted 6.35 mm to the left of the beam axis. The computation of the ΔX and ΔY values that were used to assign a t value was now altered such that the projected position from an undeflected trajectory was not correct. Consequently, the noninteracting beam particles were now assigned values mostly in t-bins 2 and 3, instead of t-bin 1. A small difference was observed in the t-bin assignment and the transmission for the two beam-polarization states. A shift in the numbers of scattered particles per t bin then changed the calculated asymmetry per t bin. For example, after the translation in position, $\epsilon_1 = 0.00187 \pm 0.00065$, compared to the value of ϵ_1 given in Table I for antiprotons. This would then affect the fit of the asymmetry as a function of t bin, and finally the background asymmetry calculation. The transmission asymmetry was affected by a different t-bin 1 asymmetry and much less by the background asymmetry. Even though the effect of the two polarization states was cumulative, the resulting asymmetry for each was dependent on how well the other two quantities cancel (snake and target states), as shown in Table III. A computer simulation showed that a displacement up to ± 2 mm changed the transmission less than 1.5%.

The observed difference in the beam-particle transmission could then be partly explained by a translation of the transmission counter. Small density differences in the target could also explain this difference in transmission between beam-polarization states and the change of transmission between the different t bins, as described below.

3. Polarized target studies

Another study was made of effects related to the polarized target that may influence the data. Proton data taken with the target solenoid located in the polarizing position, centered at the target, were compared with data when the solenoid was in the large-aperture position

of the frozen-spin mode, moved 16 cm upstream of the target center. No difference in the $\Delta\sigma_L$ asymmetry was observed. However, the pol zero asymmetry and the fake zero asymmetry both showed differences between the two solenoid positions that may be due to a difference in the position of the beam. A test to determine if the solenoid caused a small amount of beam steering was inconclusive.

Another study involving the target was made on the relative amounts of ^{3}He and ^{4}He in the target volume and how much this difference contributed to the beam transmission. A target density difference could explain the difference in the transmission between the + and − beam polarization states. At a period when the ^{3}He level within the target was low compared to normal conditions, an overall drop in the beam transmission ratio for the number of particles in t-bin 1 was observed to be 0.3%. The explanation was that since the ^{3}He level was low, there was more ^{4}He in the target, and consequently, more scattering and less transmission occurred. Thus it was possible to observe a difference in the target density. No difference was seen in the transmission rates between + and − polarization states of the beam during this test. There was also no difference observed in any of the asymmetries due to the transmission difference related to the target density. It is interesting to note that the drop in the number of particles in t-bin 1 corresponded to an increase in the number of zero and multiple hits and large-angle scatters (t-bin 12) detected by the transmission counter. This pattern occurred for both the + and − beam polarization states. A small difference in the transmission was also observed when detectors and other material were removed from the beam line.

4. N- and S-type scattering asymmetries

An analysis was performed to determine asymmetries using the beam polarized in the N direction, which is vertically perpendicular to the beam axis. A left-right asymmetry was calculated from the following relation,

$$\epsilon_{LR} = \frac{(L_+ + R_-) - (L_- + R_+)}{(L_+ + R_-) + (L_- + R_+)}\,, \tag{13}$$

where L and R are the normalized number of particles detected in the transmission counter to the left and right, respectively, of the undeflected beam-particle trajectory, as defined by the ΔX value, and + and − correspond to the up or down spin orientation of the particle. The terms L_+, R_-, etc. contain contributions from both the snake and pol states. Due to the method in which the scattered particles were assigned, the quantity ϵ_{LR} is sensitive to a +N spin in that portion of the beam tagged with positive polarization, and to a −N spin for the negative polarization (or vice versa). The asymmetry ϵ_{LR} is not sensitive to S-type or L-type spin components in the nominal N-type beam, or to equal amounts of a +N (−N) spin component in both the + and − parts of the beam. The up-down asymmetry ϵ_{UD} was formed in an analogous manner to Eq. (13) by substituting U and D for L and R. The value of ϵ_{LR} gives a "type" of Coulomb-nuclear interference measurement of elastic scattering, which should produce a nonzero left-right asymmetry and a zero up-down asymmetry. The data are presented in Table V for protons and antiprotons. The ϵ_{LR} value for protons showed a significant asymmetry, a 13σ effect, and for antiprotons, a smaller 5σ effect. The results for ϵ_{UD} for both protons and antiprotons were consistent with zero. These results clearly show that there was a large asymmetry from a polarized beam in the expected manner.

Values of ϵ_{LR} and ϵ_{UD} were also calculated using the tagged zero polarization beam particles. A large left-right asymmetry was found, and that was again consistent with a translation of the transmission counter and beam motion. A similar effect was also observed in the up-down asymmetry for the tagged zero polarization particles.

A further investigation of this analysis compared these results with the actual CNI measurement performed in this beam line. In Ref. [42], the analyzing power decreased by several percent as a function of $-t$, in the region $-t \geq 3 \times 10^{-3}\,(\mathrm{GeV}/c)^2$. The data accumulated in the CNI-like measurement are displayed in Table VI, where the $-t$ value is the average of a range of several t bins, and ϵ_{LR} is the left-right asymmetry calculated in this range. The data indicate a decreasing asymmetry, which is related to the analyzing power, as a function of increasing $-t$. These data followed the general trend of the t dependence given in the CNI results. The same t dependence was found for the antiproton beam data, but

the measured asymmetries were not as large. The up-down asymmetries as a function of $-t$ were consistent with zero.

This same N-type spin analysis using the left-right and up-down asymmetry calculations was performed on all the longitudinally-aligned spin data. The results are shown in Table V, and indicate a nonzero left-right asymmetry for both the proton and the antiproton data. A similar effect can be observed for the up-down asymmetries. These nonzero values could be due to N- and S-type spin components in the beam, but could also be due entirely to detector misalignment, beam motion, and the wrong assignment of t-bin values. If the effect in ϵ_{LR} was due entirely to an N-type component, an angle showing the maximum amount of rotation of the polarization vector from purely L-type beam could be calculated. These were found to be $(4.1 \pm 0.8)^\circ$ for protons, and $(-6.4 \pm 2.9)^\circ$ for antiprotons. Calculations from a Monte Carlo program using the observed beam motion and misalignment give approximately the same value for ϵ_{LR}.

5. Other tests

Another test of the beam had the primary production target, which produced the Λ hyperons for the polarized protons, removed from the primary 800-GeV/c proton beam. Less than 2% of the amount of the original beam remained as a background. This indicated that there were no significant secondary sources in the beam line.

An observation was made that the beam made a slight horizontal angle relative to the center line of the beam-tagging hodoscopes that provide the measurement of the beam polarization. This angle caused slightly more beam particles to be tagged with a positive polarization at higher momenta, and slightly more with negative polarization at lower momenta. If the transmission asymmetry was correlated with the momentum, then a false asymmetry could result. This effect, however, cancels when the snake magnets are reversed.

Some on-line studies were made of the quality of the data related to beam intensity. A high beam intensity caused unstable conditions with the electronic trigger and hardware. It

was also found that the data exhibited variations outside of statistics. Due to these problems, the intensity of the polarized beam was set at an average of 6.2×10^6 particles per spill for protons, and 4.2×10^6 particles per spill for antiprotons, even though the beam line was capable of a much higher intensity. From the data taken within this intensity boundary, no correlation was observed between intensity and the calculated asymmetries. Tests were also made by adjusting a collimator, located upstream of the beam-tagging region. Opening the collimator increased the intensity of the beam, but most of this increase was due to background as indicated by the increase in particles vetoed in the trigger by the beam Čerenkov counter. The second transmission counter and the *SBF* logic were less sensitive to rate effects.

Events taken during the 10-Hz sampling rate included much information that was not available from the data accumulated with the scalers. These data included momentum, polarization, and particle hit distributions, all as a function of the snake and pol states. The particle hit distributions showed the expected pattern of the + and − beam polarizations being on opposite sides of the beam spot horizontally, with the zero polarization state between the two. The horizontal spatial difference between the + and − beam polarization centroids was about 5 mm at the transmission counter. It also showed that the beam size was decreasing due to focusing at the target. The momentum distribution showed fewer particles at the higher momentum values, and a vertical spatial difference of about 4 mm from low to high momenta at the transmission counter. There were also less than 2% differences in the average momentum values between the two snake states and the two beam polarization states. In most of the distributions, there was little or no difference between the proton and antiproton beam data. The data sampled on-line were also a productive diagnostic tool for understanding experimental effects in the off-line analysis.

As discussed previously, the data were read by the computer a total of 11 times during a beam spill. Asymmetries were calculated for several different reads of the data to check for any variations that may occur during the spill. No significant variations from the average spill asymmetry were observed during these reads. The first data read was observed to

contain about one-third the number of particles in it compared to the other reads.

Most of the tests for systematic errors indicate that the observed results will have no significant effect on the measured data. This is primarily due to the cancellation of asymmetries by reversing the spin state. Most of the observed effects on the false asymmetries could be explained by these many tests.

E. Calculation of $\Delta\sigma_L$ and the systematic error

The data were accumulated in several groups, each group containing approximately 30 hours of data during one polarized target state. The data fell naturally into these groups; each spill contained particles with both + and − beam-polarization states, and the snake state reversal occurred every 12 spills. Asymmetries were calculated for each group of data, and the $\Delta\sigma_L$ transmission, fake zero, fake rotation, and parity asymmetries are given per group for protons and antiprotons in Table VII. The effect of changing the target state can be observed in Table VII. For example, the ϵ_R asymmetries for each group of data are very large, yet when all the group data are taken into account, they cancel fairly well.

As discussed previously, the two quantities, fake zero and fake rotation asymmetries, give an effectively unpolarized beam and target when averaging over the entire data sample. The asymmetries for these two quantities should therefore be zero since there is no spin enhancement in any state. However, for the groups in Table VII there is no average over the target states. In this case, ϵ_F corresponds to an average over the pol states, but a single snake and target state, and ϵ_R corresponds to an average over the snake states, but a single pol and target state. Thus, ϵ_F is sensitive to effects caused by snake state differences, such as the beam motion described earlier, and ϵ_R is sensitive to pol state differences, such as the varying transmission across the beam spot. In an ideal experiment, both ϵ_F and ϵ_R would be zero. If either or both ϵ_F and ϵ_R are nonzero, the data can be corrected using the correlation of these asymmetries with the $\Delta\sigma_L$ transmission asymmetry, ϵ. The differences in ϵ before and after the corrections then give an estimate of the systematic error.

Table VIII shows the uncorrected $\Delta\sigma_L$ transmission asymmetries per group for protons and the total χ^2 from each of the group data points. Correlations were made between the transmission asymmetries per group and the fake zero and fake rotation asymmetries per group. The transmission asymmetries were corrected using a straight-line fit of the correlation and finding the values of ϵ when the other two asymmetries were set to zero. Table VIII also shows the corrected values and the χ^2. Using these corrected asymmetries, the target constant, and the average beam and target polarizations per group, the values of $\Delta\sigma_L(pp)$ could be calculated, along with a weighted average of these values. An estimate of the systematic error was then made by correcting the statistical error by $\sqrt{\chi^2/\mathrm{df}}$ to obtain a total error, and from this total error derive the systematic error. The experimental result is: $\Delta\sigma_L(pp) = -42 \pm 48\,(\mathrm{stat.}) \pm 53\,(\mathrm{sys.})\,\mu\mathrm{b}$. The systematic and statistical errors are approximately equal, and the value did not change by more than 1σ after the corrections.

The same analysis can be performed using the antiproton beam data. The uncorrected and corrected data are presented in Table IX for each group data point, along with the total χ^2 and $\Delta\sigma_L$ values. The result is: $\Delta\sigma_L(\bar{p}p) = -256 \pm 124\,(\mathrm{stat.}) \pm 109\,(\mathrm{sys.})\,\mu\mathrm{b}$. Again, the statistical and systematic errors are comparable, and the value of $\Delta\sigma_L$ hardly changed after the corrections.

No corrections [52] were made to the data for Coulomb-nuclear interference, known to be significant at lower energies. For this measurement, the corrections were calculated to be a few microbarns, which is small compared to the other uncertainties.

F. Comparison of $\Delta\sigma_L$ theoretical models

Two theoretical models offer predictions for $\Delta\sigma_L(pp)$. One model is based on conventional Regge phenomenology and the other comes from phenomenology of jet physics. There are no published theoretical predictions for $\Delta\sigma_L(\bar{p}p)$.

The model [53] based on conventional Regge phenomenology has the A_1 pole as the leading singularity with unnatural parity that can couple to the t-channel, unnatural-parity

exchange amplitude, U_0, at $t = 0$. Unitarity relates $\Delta\sigma_L(pp)$ to the imaginary part of this scattering amplitude by $\Delta\sigma_L(pp) = (8\pi/k)\,\mathrm{Im}\,U_0$, and $U_0 = \frac{1}{2}(\phi_1 - \phi_3)$, as described in Eqs. (1) and (2). If U_0 has coherent Regge behavior in this region, then $\Delta\sigma_L(pp) \approx c\,p_{lab}^{\alpha-1}$, where α is the intercept of the A_1 trajectory and has the value of -0.15, p_{lab} is the laboratory momentum, and c is a constant normalized to the $\Delta\sigma_L(pp)$ values with p_{lab} between 4 and 11.75 GeV/c. Extending this to a laboratory momentum of 200 GeV/c, the estimate becomes $\Delta\sigma_L(pp) \approx -20\,\mu$b.

The other model [54] includes contributions from hard, pointlike scattering mechanisms and soft, coherent dynamics to form $\Delta\sigma_L(pp)$, and by measuring the hard-scattering contribution, information on the spin-dependent quark and gluon distributions within the polarized proton can be obtained. The quantity $\Delta\sigma_L$ can be decomposed into two parts: $\Delta\sigma_L(pp;s) = \Delta\sigma_L^{soft}(pp;p_0,s) + \Delta\sigma_L^{jet}(pp;p_0,s)$, where $\Delta\sigma_L^{soft}$ is the contribution from coherent hadron dynamics, $\Delta\sigma_L^{jet}$ is due to the pointlike contribution from the scattering of quarks and gluons, p_0 is the momentum cutoff parameter distinguishing the two parts, and s is the square of the c.m. energy. A measure of the energy dependence of $\Delta\sigma_L^{jet}$ for a fixed cutoff parameter can provide new information concerning the energy regime where the hard-scattering approximation is valid. The value of $\Delta\sigma_L^{jet}$ can be sensitive to the spin-dependent gluon distribution in a polarized proton, ΔG, and can differentiate between no, small, or large ΔG values.

Two estimates of $\Delta\sigma_L^{jet}$ are given here, one with a large ΔG value and the other with $\Delta G = 0$. Using $p_0^2 = 5\,(\mathrm{GeV}/c)^2$ and $\sqrt{s} = 20$ GeV for both estimates, $\Delta\sigma_L^{jet} \approx 26\,\mu$b for $\langle\Delta G\rangle = 6$, and $\Delta\sigma_L^{jet} \approx 2\,\mu$b for $\langle\Delta G\rangle = 0$. Note that the predicted values of $\Delta\sigma_L^{jet}$ are positive in this model, while the prediction using Regge phenomenology is negative at 200 GeV/c. An estimate of $\Delta\sigma_L^{jet}(\bar{p}p)$ will be approximately the same as that for $\Delta\sigma_L^{jet}(pp)$, regardless of which gluon model is used. For large ΔG, the contributions of the different scattering processes to $\Delta\sigma_L^{jet}$ are dominated by gluons, which contribute the same amount to both of the p-p and $\bar{p}$-p cross sections. For $\Delta G = 0$, the difference in the cross sections is dominated by the valence quark contributions, but this difference is on the order of a

fraction of a μb, depending on p_0, which is likely to be much smaller than either total cross section [55].

Figure 13 shows the experimental values of $\Delta\sigma_L(pp)$ and $\Delta\sigma_L(\bar{p}p)$ at 200 GeV/c, including the statistical and systematic errors, and the theoretical predictions for $\Delta\sigma_L$ and $\Delta\sigma_L^{jet}$. The experimental data for both $\Delta\sigma_L(pp)$ and $\Delta\sigma_L(\bar{p}p)$ are consistent with zero within the errors. From this summary, the experimental data points for $\Delta\sigma_L$ at 200 GeV/c are not able to differentiate between the two theoretical models, or between no or large ΔG contributions to the proton spin in $\Delta\sigma_L^{jet}$. A more precise measurement of $\Delta\sigma_L$ at a higher energy may be able to do this. The sign and the magnitude of $\Delta\sigma_L(pp)$ are consistent with the asymptotic energy dependence of the Regge amplitudes proposed to explain the values at 6 and 11.75 GeV.

One motivation for this measurement, described in Sec. I, was to investigate to what extent the helicity-changing amplitudes participated in the rise of the unpolarized, total cross sections. Since the value of $\Delta\sigma_L$ is consistent with zero for both p-p and $\bar{p}$-p scattering at 200 GeV/c, it appears that this rise in the cross section is not due to spin effects. Another motivation was that $\bar{p}$-p interactions may result in significant polarization effects due to the dependency on the helicities of the annihilation of two spin-1/2 particles into vector intermediate states. Again, because $\Delta\sigma_L(\bar{p}p) \approx 0$, this dependence does not seem strong. Finally, since $\Delta\sigma_L$ is related to the helicity amplitudes, as given in Eq. (1), and the value is $\Delta\sigma_L \approx 0$, then $\mathrm{Im}\,\phi_1(0) \approx \mathrm{Im}\,\phi_3(0)$ at 200 GeV/c.

V. PARITY NONCONSERVATION

A. Introduction

Parity conservation requires that no asymmetry should be observed in the scattering of a longitudinally-polarized beam incident on an unpolarized target. That is, if parity is conserved, the cross section cannot depend on whether the particle helicity is positive or

negative. A measurement of the longitudinal-polarization asymmetry, A_L, can detect parity nonconservation since A_L involves terms that change sign under the parity operator. The quantity A_L is defined as

$$A_L = \frac{1}{\mid P_B \mid} \frac{\sigma^+ - \sigma^-}{\sigma^+ + \sigma^-} , \tag{14}$$

where P_B is the longitudinal beam polarization and $\sigma^{\pm}$ are the cross sections when the spin direction is parallel (+) or antiparallel (−) to the beam momentum. Experimental knowledge of the strangeness-conserving hadronic weak interaction can be gained through parity-nonconservation experiments.

Previous experiments of A_L at five kinetic energies between 13.6 MeV and 5.1 GeV have been performed using beams of polarized protons incident on unpolarized targets. The first [56] of these used 15-MeV polarized protons on a liquid-hydrogen target and found $A_L = -(1.7 \pm 0.8) \times 10^{-7}$. The second [57] was at 5.1 GeV and used a water target. The value measured was $A_L = +(26.5 \pm 6.0 \pm 3.6) \times 10^{-7}$. The third measurement at 800 MeV used both a water target and a liquid-hydrogen target. The value [58] of A_L for polarized protons on the water target was $A_L = +(1.7 \pm 3.3 \pm 1.4) \times 10^{-7}$, and the value [59] using the liquid-hydrogen target, $A_L = +(2.4 \pm 1.1 \pm 0.1) \times 10^{-7}$. The high-precision measurement [60] at 45 MeV used a polarized-proton beam and a liquid-hydrogen target to obtain $A_L = -(1.50 \pm 0.22) \times 10^{-7}$. The most recent measurement [61] was at 13.6 MeV and found $A_L = -(1.5 \pm 0.5) \times 10^{-7}$. All of these measurements were dedicated experiments that acquired data for several years and had expended much effort to reduce systematic errors. The value of A_L at 5.1 GeV is noted to be much larger than the others.

The experimental data at the lower energies can be described reasonably well with the theoretical predictions based on a meson-exchange model [62–71] and a hybrid-quark model [72]. The meson-exchange model has one to two meson exchanges between a parity-conserving, strong interaction vertex and a parity-nonconserving, weak interaction vertex. At energies below a few hundred MeV in p-p elastic scattering, the parity-conserving interaction is described by meson-exchange potentials, while the parity-nonconserving interaction

is described by several meson-nucleon coupling constants. The predictions give $A_L \sim 10^{-7}$. Other theoretical calculations are based on the multiperipheral model [73], and heavy-boson exchange [74].

At higher energies, a quark-model calculation [75,76] of A_L shows that the dominant contribution comes from the parity-nonconserving interaction of two quarks from the same beam proton that may be described as a mixing of the beam protons into intermediate states of negative parity. This higher-twist subprocess dominating the high-energy asymmetry can be approximated in the parton model as quark-vector diquark scattering. A vector diquark from the polarized proton (unpolarized target) interacts strongly with a quark from the unpolarized target (polarized beam) with the parity-nonconserving weak interaction occurring only between the quarks of the vector diquark. The asymmetry contains soft processes with poorly-known individual parameters, so the normalization needs to be fixed by experimental data. Once this is fixed, all of the uncertainty in the asymmetry is due to a parameter b, which effectively represents the rate of scale variation of the strength of the QCD coupling. By fixing the normalization to the 5.1-GeV data point, the theoretical prediction at 800 MeV matches the experimental value fairly well. This calculation predicts a value of $A_L \sim 10^{-4}$ at a laboratory momentum of 200 GeV/c for $b = 1.4$.

The energy dependence of A_L from this model had been criticized [77] for not using the proper normalizing cross section in the calculation. The A_L values would then be $\leq 2 \times 10^{-7}$ for energies up to 500 GeV. However, this criticism was refuted [76] by the original authors of the model stating that the calculations used in the criticism did not use a running coupling constant nor a complete set of graphs, and did not properly implement gauge invariance.

Another theoretical prediction [78] at high energies uses the parity-nonconserving, nucleon wavefunction effect to calculate an asymmetry. This is accomplished by adding a weak-interaction amplitude from the interaction of $W^{\pm}$ and Z^0 bosons to the strong interaction amplitude. These vector bosons are exchanged between the three quarks of a single nucleon. The high-energy limit of the asymmetry due to wavefunction renormalization is given by $A_L^{wf} = (p_{lab}/E_{lab})\, C_N$, where $C_N = 2.16 \times 10^{-6}$ for protons and takes into account

contributions from different diagrams. This formula [79] is also valid for the $\bar{p}$-p process because the elastic $\bar{p}$-p amplitudes can be described in terms of the same Regge exchanges up to a sign. The predicted value for both $A_L(p)$ and $A_L(\bar{p})$ at 200 GeV/c is then 2.16×10^{-6}. This model has also been criticized [77,80–82] because the energy dependence is too weak, so that at lower energies it has much larger A_L values than the experimental data.

None of the theoretical approaches can accurately portray the energy dependence of A_L over the entire range of measurements. The meson-exchange model reasonably describes the experimental results up to 800 MeV, but underestimates the 5.1-GeV result. The higher-energy quark model predicts the data at 800 MeV and 5.1 GeV, but is not applicable at low energies.

B. Derivation of the Parity-Nonconserving Asymmetry, A_L

In this experiment at high energy, the same method using corrections to the $\Delta\sigma_L$ transmission asymmetry from the first transmission counter could also be used to obtain a value for the parity-nonconserving parameter, A_L. The sums, as shown in Fig. 11, are arranged in the asymmetry calculation to give an effective unpolarized target. The states (b), (c), (f), and (g) in Fig. 11 were used in the "parallel" sum. The asymmetries ϵ_P per group that measure the parity are given in Table X. The magnitudes of the asymmetries are identical to those for $\Delta\sigma_L$ because the same sums are used in both calculations, but the signs are sometimes different in the case of $\Delta\sigma_L$ to account for the polarized target spin. The uncorrected and corrected asymmetries are given in Table X for each group, along with the total χ^2 and A_L values. The corrections were made to the $\Delta\sigma_L$ data, but the appropriate signs were changed in the corrected asymmetry of $\Delta\sigma_L$ to form the corrected parity asymmetry. The average magnitude of the beam polarization per group was used with the corrected ϵ_P to calculate the individual A_L values. The systematic error was calculated in the same fashion as described in the $\Delta\sigma_L$ analysis. The experimental result for parity nonconservation in proton scattering is: $A_L(p) = +[5 \pm 17\,(\text{stat.}) \pm 20\,(\text{sys.})] \times 10^{-6}$, which is consistent

with zero.

Using the same analysis for A_L with the antiproton beam data as that for protons, the uncorrected and corrected data, total χ^2, and A_L values per group are presented in Table XI. The result for parity-nonconservation in antiproton scattering is: $A_L(\bar{p}) = +[22 \pm 46\,(\text{stat.}) \pm 55\,(\text{sys.})] \times 10^{-6}$. This result is also consistent with zero.

Figure 14 compares the $A_L(p)$ result from this experiment with the previous measurements of A_L at lower energies. The curves represent the theoretical predictions of A_L from the quark model [75,76] with different values of the parameter b. The theoretical prediction from the wavefunction renormalization model [79] would appear in Fig. 14 as a horizontal straight line close to the value of zero. The predictions based on meson-exchange models [62–71] would also be displayed as a line very close to zero.

The target material used in this experiment was pentanol, as described in Sec. II B. The hydrogen fraction of pentanol is 13.6%, compared to 11.1% for the water target used in Ref. [57]. Since the hydrogen fraction is nearly the same for both, the present results of A_L at 200 GeV/c can be compared more directly with those presented in Ref. [57] at 6 GeV/c (5.1 GeV).

It has been shown [83] that nuclear shadowing effects significantly reduce the values of A_L as a function of the atomic weight, A. This Glauber model calculation gives a dependence as $A_L(\overrightarrow{p}\,A) \sim A^{\frac{1}{3}}$, and a suppression for a water target as $A_L(\overrightarrow{p}\,N) \approx 1.7\,A_L(\overrightarrow{p}\,H_2O)$ for incident proton energies below 5–10 GeV. For higher energies, inelastic shadowing corrections become important and the dependence becomes $A_L(\overrightarrow{p}\,A) \sim A^{-0.09}$. It should also be noted that the extra, nonhydrogen nucleons do not influence the measurement of $\Delta\sigma_L$ because they are unpolarized, and any effect will cancel when the target spin is reversed. However, in the parity measurement, the nucleons would be included in any effect since there is no target spin reversal.

A measurement of parity nonconservation could also be made using an unpolarized proton or antiproton beam on the polarized target, giving values for $A_L(p\overrightarrow{p})$ or $A_L(\bar{p}\overrightarrow{p})$, respectively. Averaging over the beam polarization to produce an effectively unpolarized

beam on a polarized target would give similar results. However, any effect would be greatly diluted because the fraction of polarized protons is only 13.6% of the total target material. Therefore, a much longer data-taking period would be necessary to achieve the same statistical error as that on $A_L(\overrightarrow{p}p)$ or $A_L(\overrightarrow{\overline{p}}p)$.

C. Systematic Effects on the A_L Results

The experimental method used in this experiment, which differed from previous A_L measurements, was less sensitive to certain systematic effects that could cause a fake, nonzero value of the asymmetry. Several examples of these effects include: (1) inelastic reactions from polarized-beam particles with transverse spin components, (2) transverse residual polarization, (3) parity-nonconserving decays of secondary particles, and (4) beam-matter interactions.

The first example of inelastic reactions from polarized-beam particles would produce slowly-varying asymmetries over a wide range of scattering angles that would be detected in the transmission hodoscope. These events would appear in the analysis as a contribution to the background asymmetry, ϵ_B, and would be subtracted from the transmitted-beam events, as described in Sec. III. Hence, these decays should not affect the value of A_L in this experiment.

The second example of transverse residual polarization effects is not expected to cause sizeable systematic effects. Transverse residual polarization is described in Ref. [84] and occurs when there is a scattering of particles with opposite transverse spin components in the tails of opposing sides of the beam profile, coupled with a finite detector acceptance. In particular, a transverse spin component near the edge of the beam spot is not expected to cause a large systematic error. The detector geometry of the SNA1, SNA2, and TRA hodoscopes and the target and muon veto counters provides full acceptance for all scattered particles with $-t \leq 0.024\,(\mathrm{GeV}/c)^2$, and a slowly-decreasing acceptance beyond that to the largest $-t$ measured. The background subtraction should nearly cancel these effects.

The third example of parity-nonconserving decays of secondary particles, such as Λ^0 and $\overline{\Lambda^0}$ hyperons, again would produce a broad range of scattering angles. Any effect would be a contribution to the background asymmetry, and subtracted from that of the transmitted beam. Again, this should not affect the value of A_L.

The final example of beam-matter interactions is discussed in Ref. [57], and in this experiment would be the scattering of beam particles upstream of the snake magnets, where the beam-polarization direction is horizontally-transverse (S-type spin direction) and would affect the number of particles accepted by the trigger. Since the trajectory of each beam particle was followed before and after the target, only those particles that pass the $\Delta\sigma_L$ trigger requirements were selected for further analysis. Therefore, this type of event is not expected to change the measurement of the transmission or A_L.

Some systematic errors, which canceled during the measurement of $\Delta\sigma_L$ when the target polarization was reversed, may affect the asymmetry A_L, when data from the two target polarization states are added together. These systematic errors for A_L, but not for $\Delta\sigma_L$, can be made from the combined effects of two or more of the following conditions: (1) beam motion correlated with the snake state, (2) a spatial offset of the hodoscope centers from a straight line, (3) a difference in the beam transmission with position or polarization state, and (4) a transverse spin component in the beam polarization direction. An example of these combined effects could be an N-type spin component of the beam, which would produce a left-right asymmetry due to the parity-conserving elastic scattering in the CNI region, and hodoscope offsets (or beam motion) perpendicular to the transverse spin component of the beam. The result could then be a spurious asymmetry. These combined effects might not be completely subtracted with the background, since the CNI analyzing power changes rapidly (see Table V and Ref. [42]) at small $-t$, especially for $-t \leq 0.02\,(\mathrm{GeV}/c)^2$. Such combinations of effects have not been well-studied experimentally, and their influence on the A_L results, if any, is not known. Very crude estimates suggest that such combined systematic effects are no greater than the quoted systematic error.

Detailed knowledge of the transverse spin components in the nominal L-type beam is

unfortunately limited. The main reason for this lack of information is that there are no known high-rate reactions with large analyzing powers at these energies that would allow a determination of the small spin components in reasonable data-taking periods. As a comparison, the CNI-like measurements described in Sec. IV D and Table V give estimates of the magnitudes of the transverse spin components at the 5σ level based on many weeks of data collection.

Several possible mechanisms for producing transverse spin components in an L-type polarized beam have been considered. These mechanisms include: (1) wrong electrical currents in the snake magnets, (2) momentum-dependence of the acceptance and production cross sections for the protons (antiprotons), (3) asymmetric up-down proton (antiproton) acceptance in the beam line, and (4) fringe fields from the beam-line magnets. Other effects were considered to cause transverse spin components, but most of these would be expected to give a negligible value for the asymmetry. Combinations of two or more of these effects are also expected to be very small.

The first mechanism for producing a transverse spin component is due to the wrong electrical current in the snake magnets. This condition would cause an improper rotation from S-type to L-type beam spin direction. The error in the snake magnet current was estimated to be a maximum of 1% for all magnets or 0.5% from magnet to magnet. A 1% error in the magnet current could produce an S-type spin component with a magnitude of approximately 4% of the nominal L-type spin, and a much smaller N-type spin component. The direction of the S-type beam component would be opposite for the positively- and negatively-polarized parts of the beam spot, and the direction would remain unchanged upon reversal of the snake. Thus, the asymmetry ϵ_{UD}, whose values are listed in Table V would not be sensitive to this S-type spin component because the opposite state does not contribute.

The second mechanism combines the effects from the momentum acceptance for decay protons (antiprotons) and the nonuniform, momentum-dependent cross sections for producing Λ ($\overline{\Lambda}$) hyperons. These effects could produce a small, net L-type spin component to the

selected beam particles at the production target. An estimate was made of the magnitude of this L-type component, taking into account the relativistic transformation of the phase space and the spin direction of the proton, and was determined to be about 2%. This L-type spin component results in a small S-type component after the spin rotation by the snake magnets, and the direction of the S-type component is the same for both of the polarized + and − parts of the beam. As before, the asymmetry ϵ_{UD} would not be sensitive to this component. The small L-type spin component at the production target would have remained as an L-type component when the snake magnets were used to produce an N-type beam.

The third mechanism is due to an asymmetric up-down acceptance for protons (antiprotons) due to the vertical bends in the beam line and a possible "scraping" of the beam on vertical apertures. Such an acceptance would have given a small N-type component to transmitted beam particles at the production target. A small N-type component would remain after the snake magnet spin rotation, and this component would be in the same direction for both the + and − polarization states of the beam. This direction does not change sign with snake reversals. The left-right asymmetry ϵ_{LR} would not be sensitive to this transverse spin component. When the snake magnets rotated the beam-spin direction to N-type, this small N-type component would be rotated to an L-type one, and this component cannot be observed with the CNI-like measurements.

The last mechanism considered to produce a transverse spin component is the effect of fringe fields from the beam-line magnets on the spin direction of the beam particles. These effects are calculated to be small due to the details of the magnet design, and in addition, the effect of the longitudinal field integral on the spin precession is small due to a factor of $1/\beta\gamma$ of the beam.

The experimental method used would mostly cancel systematic effects in A_L from the sources of transverse spin considered above. When the transverse spin components are in the same direction for + and − beam-polarization states, then the effect mostly cancels when the difference in transmission for the two beam-polarization states is taken for a given snake state. If the transverse spin components do not change with the snake state, then the effect

largely cancels when the difference in the transmission between the two snake states is taken. In summary, all of the mechanisms considered to produce an N-type or S-type transverse spin component in the beam polarization would not be measurable using the asymmetries ϵ_{LR} and ϵ_{UD} in Table V, and also would not make a contribution in A_L. The nonzero values for these asymmetries in Table V are then most likely due to the combined effects of the beam motion with snake state and hodoscope misalignment.

The fake zero asymmetry ϵ_F and the fake rotation asymmetry ϵ_R may also be sensitive to transverse spin components in the beam. However, the first and third mechanisms for producing these components do not reverse the spin direction with snake state, and thus should cancel in the asymmetry ϵ_R. Likewise, the second and third mechanisms lead to the same spin direction for the + and − pol states, and thus cancel in ϵ_F. As a result, ϵ_F may be sensitive to transverse spin components caused by incorrect snake magnet currents, while ϵ_R may be sensitive to transverse spin components caused by a small, net L-type spin of the selected beam particles at the production target.

D. Parity-Nonconserving Asymmetry Results

The experimental results of the parity-nonconserving asymmetry A_L presented here are the first ones in the hundred-GeV range and the first ever involving antiprotons. Both of the $A_L(p)$ and $A_L(\bar{p})$ results are consistent with zero and, compared to the previous A_L measurements, have relatively large errors assigned to them. Taking into account these conditions, it is interesting to observe that the values of $A_L(p)$ and $A_L(\bar{p})$ at 200 GeV/c both are positive, along with the measurements of A_L at 800 MeV and at 5.1 GeV. These are all of the higher-energy measurements. Since the target material used here is pentanol, the contribution of nuclear effects is expected to dilute the measured asymmetry by approximately a factor of 1.5 at high energies.

The experimental results of $A_L(p)$ and $A_L(\bar{p})$ can be compared to the two theoretical predictions at high energy, described previously. The quark model calculation [75,76] predicts a

value for $A_L \approx 35 \times 10^{-6}$ for the parameter $b = 4.0$, 95×10^{-6} for $b = 1.4$, and 177×10^{-6} for $b = 0.4$ at 200 GeV/c. The experimental value of $A_L(p) = +[5 \pm 17 \pm 20] \times 10^{-6}$ is about 1.4σ, 3.7σ, and 7σ below the predictions for b values of 4.0, 1.4, and 0.4, respectively. The predictions using the smaller values of b tend to be farther from the experimental value, and values of $b < 1.4$ seem to be excluded. The entire set of predictions in this model is normalized to the data point at 5.1 GeV/c, so if this normalization was incorrect, the predicted energy dependence could become proportionally smaller. The second prediction at 200 GeV/c used wavefunction renormalization [78,79] to predict a value of $A_L = 2.16 \times 10^{-6}$ for both $A_L(p)$ and $A_L(\bar{p})$. Both of the measured experimental values are consistent with the predictions of this model.

The experimental detectors and method used in this experiment has differed from that of the previous measurements of the parity-nonconserving asymmetry. Some of these differences include the tracking of individual particle scatters to determine the transmission, an extrapolated background subtraction in the data analysis, and the use of other asymmetries to correct for possible systematic effects. This experimental arrangement and method provide some advantages for the measurement, and also contains a different set of systematic errors. Not all of these systematic effects were able to be measured in this experiment, such as the transverse spin components in the beam, but an attempt was made to identify those that had caused problems with past measurements and to estimate the magnitude of the effects on this present measurement of A_L. Past experiments also used a liquid-hydrogen target, whereas this experiment had no opportunity to acquire data with both a liquid-H_2 target and the detector system in place.

Typically, a measurement of the parity-nonconserving asymmetry takes data for several years and many improvements are made to the experiment during this time to enhance the data quality and eliminate systematic errors. The present measurement of A_L in this experiment had a limited time of approximately two months to acquire data with no opportunity to improve the data quality.

VI. SUMMARY

Results are presented for the differences between p-p and also $\bar{p}$-p total cross sections in longitudinal spin states $\Delta\sigma_L$, and the parity-nonconserving parameters, A_L, in total cross sections for longitudinally-polarized beams of protons and antiprotons at 200 GeV/c. These data are at a significantly higher energy than other polarized-proton beam results for these quantities, and they are the first such measurements with polarized-antiproton beams at any energy. Because the measurements were at a higher energy compared to earlier experiments, some new experimental techniques were required.

The $\Delta\sigma_L$ results are both consistent with zero: $\Delta\sigma_L\,(pp) = -42 \pm 48\,(\text{stat.}) \pm 53\,(\text{sys.})\,\mu\text{b}$ and $\Delta\sigma_L\,(\bar{p}p) = -256 \pm 124\,(\text{stat.}) \pm 109\,(\text{sys.})\,\mu\text{b}$. Many tests were performed to investigate how possible systematic errors could affect the data. Two transmission counters using different electronics and different data analysis methods were used to verify the experimental results.

The measurements of $\Delta\sigma_L$ using the two different transmission counters have not been combined because this would require a more precise understanding of the statistical correlation between the two sets of data. The correlation is strong and the statistical error of the combined result would not be much less than the value from the single measurement with the smaller error. The results presented are from the method that has the lower statistical error and that has corrections for the systematic errors.

The value of $\Delta\sigma_L$ has been shown in Eq. (3) to be related to the forward amplitudes. Compared to lower energies, the experimental values of the imaginary parts of the forward p-p elastic amplitudes, $\text{Im}\,\phi_1(0)$ and $\text{Im}\,\phi_3(0)$, are converging. These quantities are equal to within about 0.5% and 1.4% for p-p and $\bar{p}$-p interactions, respectively, at 200 GeV/c.

The result for $\Delta\sigma_L\,(pp)$ suggests that spin effects correspond to less than 15% of the rise in the total cross section from its minimum value. It is consistent with an extrapolation of lower-energy data based on Regge predictions, including or excluding $\Delta\sigma_L^{jet}$ effects. On the basis of extensive tests of systematic effects, smaller combined statistical and systematic

uncertainties are achievable with the present experimental technique. However, uncertainties of $\pm 5\,\mu$b would be desirable to distinguish between these possibilities, and this would require prohibitive amounts of time for data acquisition with the present beam intensity.

The spin effects that might occur in $\bar{p}$-p annihilation seem to correspond to at most 0.29 mb in the total cross section, or approximately 12% of the annihilation cross section at 200 GeV/c. Presumably the quark-antiquark annihilation process into massless vector gluons is not dominant at these energies, or its effects are largely canceled by other processes. Additional time for data acquisition would provide a significantly improved estimate on this fraction. Furthermore, since this is the only measured value of $\Delta\sigma_L(\bar{p}p)$, additional measurements at different energies would be quite valuable in understanding the results.

Values of the parity-nonconserving parameter A_L were derived from the $\Delta\sigma_L$ data by averaging over the target polarization. The results are: $A_L(p) = +[5 \pm 17\,(\text{stat.}) \pm 20\,(\text{sys.})] \times 10^{-6}$ and $A_L(\bar{p}) = +[22 \pm 46\,(\text{stat.}) \pm 55\,(\text{sys.})] \times 10^{-6}$, where the target has approximately the same fraction of free protons as water; both are consistent with zero. The traditional method for measuring A_L involves integrating over large numbers of particles and taking data for many years to study and minimize systematic effects, rather than the method used here, which counted individual beam particles and took data for only a few months. As a result, these data have larger uncertainties than measured values at lower energies. However, very large ($\geq 10^{-4}$) $A_L(p)$ values at 200 GeV/c are excluded by these measurements to a high probability. The results are consistent with predictions for proton-nucleon interactions using the quark model of Refs. [75,76], for the larger values of parameter "b," and with the prediction using the wavefunction renormalization model of Refs. [78,79]. An additional amount of data would be expected to reduce the uncertainties, and could perhaps distinguish between the two predictions. The present value of $A_L(\bar{p})$ was limited by beam intensity and the amount of available time for data acquisition.

Very interesting results on total cross sections in pure helicity states have been found from this experiment. The full physics potential for polarized beams of this design has not yet been achieved. In particular, higher-precision measurements of parity nonconservation with

liquid targets over a wide energy range are quite feasible with the experimental techniques described here.

ACKNOWLEDGMENTS

The authors wish to especially thank the following individuals for their many contributions to the success of this experiment: D. Carey, R. Coleman, A. Melensek, and R. Schailley for their expertise in the beam design and development; D. Allspach, A. Buehring, D. Gacek, R. Jaskoviac, A. Passi, E. Petereit, R. Sanders, and N. Hill for engineering development; K. Schwindlein, T. Prosapio, M. Shoun, E. Weiler, J. Wilson, and J. Hoover for facility support; R. Stanek for cryogenic support; R. Allen, K. Bailey, B. H. Blair, T. Capelli, L. Crawford, J. Dyke, O. Fletcher, K. Fukuda, K. Kephart, M. Laghai, M. Modesitt, T. Morkved, A. Rask, S. Strecker, R. Taylor, and C. Woods for detector, target, and snake magnet construction; E. Vaandering for computer analysis; M. Beddo for analysis consultation; R. Mischke, J. D. Bowman, R. Talaga, and S. Vigdor for informative discussions on measurements of parity nonconservation; and G. Ramsey, D. Sivers, T. Goldman, E. Berger, and J. Soffer for helpful discussions on theoretical issues. Much thanks is also expressed for the numerous contributions by the technical staff at the many collaborating institutions. The authors express their gratitude to the staff of Fermi National Accelerator Laboratory for their assistance and support, and especially to L. Lederman for his foresight. The experiment benefited from the efforts of our colleagues, M. M. Gazzaly, R. Rzaev, N. Tanaka, and A. Villari, who have passed away; we will miss them all greatly.

Work for this project was supported by the U.S. Department of Energy, Division of High Energy Physics, Contract Nos. W-31-109-ENG-38, DE-AC02-76CH03000, DE-AC02-76ER02289, W-7405-ENG-36, DE-AS05-76ER05096, and DE-FG02-91ER40664; the Istituto Nationale di Fisica Nucleare (INFN), Italy; the USSR State Committee on Utilization of Atomic Energy (SCUAE); the Commisariat à l'Energie Atomique, France; the Ministry of Science, Culture, and Education in Japan; and LAPP-IN2P3, Annecy-le-Vieux, France.

One of us (KWK) acknowledges partial support from the Division of Educational Programs at Argonne National Laboratory, while working as a Faculty Research Participant.

REFERENCES

[1] D. L. Adams *et al.*, Phys. Lett. B **261**, 201 (1992); **264**, 462 (1991); Z. Phys. **C56**, 181 (1992).

[2] See P. M. Ho *et al.*, Phys. Rev. Lett. **65**, 1713 (1990); P. M. Ho *et al.*, Phys. Rev. D **44**, 3402 (1991); N. B. Wallace *et al.*, Phys. Rev. Lett. **74**, 3732 (1995); and references in these to previous work.

[3] See I. P. Auer *et al.*, Phys. Rev. D **34**, 1 (1986); D. G. Crabb *et al.*, Phys. Rev. Lett. **65**, 3241 (1990); and references in these to previous work.

[4] A. S. Carroll *et al.*, Phys. Lett. **61B**, 303 (1976); A. S. Carroll *et al.*, *ibid.* **80B**, 423 (1979); CERN-Pisa-Rome-Stony Brook Collaboration, *ibid.* **62B**, 460 (1976).

[5] See, for example, O. Nachtman, *Elementary Particle Physics: Concepts and Phenomena* (Springer-Verlag, Berlin, 1990), pp. 430–434.

[6] M. Jacob and G. C. Wick, Ann. Phys. (N.Y.) **7**, 404 (1959).

[7] E. Leader and R. Slansky, Phys. Rev. **148**, 1491 (1968); E. Leader, Phys. Rev. **166**, 1599 (1968).

[8] R. J. N. Phillips, Nucl. Phys. **43**, 413 (1963); S. M. Bilenky and R. M. Ryndin, Phys. Lett. **6**, 217 (1963); F. Halzen and G. H. Thomas, Phys. Rev. D **10**, 344 (1974).

[9] I. P. Auer *et al.*, Phys. Lett. **67B**, 113 (1977); Phys. Rev. Lett. **41**, 354 (1978).

[10] I. P. Auer *et al.*, Phys. Lett. **70B**, 475 (1977); Phys. Rev. D **34**, 2581 (1986); Phys. Rev. Lett. **62**, 2649 (1989).

[11] I. P. Auer *et al.*, Phys. Rev. D **29**, 2435 (1984).

[12] J. Bystricky *et al.*, Phys. Lett. **142B**, 130 (1984).

[13] J. P. Stanley *et al.*, Nucl. Phys. A **403**, 525 (1983).

[14] E. Aprile-Giboni *et al.*, Nucl. Phys. A **431**, 637 (1984).

[15] A. Th. M. Aerts *et al.*, Phys. Rev. D **17**, 260 (1978).

[16] C. W. Wong and K. F. Liu, Phys. Rev. Lett. **41**, 82 (1978).

[17] C. W. Wong, Prog. Part. Nucl. Phys. **8**, 223 (1982).

[18] P. LaFrance and E. L. Lomon, Phys. Rev. D **34**, 1341 (1986); P. González and E. L. Lomon, *ibid.* **34**, 1351 (1986); P. González, P. LaFrance, and E. L. Lomon, *ibid.* **35**, 2142 (1987).

[19] Yu. S. Kalashnikova *et al.*, Yad. Fiz. **46**, 1181 (1987) [Sov. J. Nucl. Phys. **46**, 689 (1987)].

[20] N. Konne *et al.*, Phys. Rev. D **35**, 239 (1987).

[21] T. Goldman *et al.*, Phys. Rev. C **39**, 1889 (1989).

[22] R. L. Shypit *et al.*, Phys. Rev. Lett. **60**, 901 (1988); **61**, 2385 (1988); Phys. Rev. C **40**, 2203 (1989).

[23] D. V. Bugg, Ann. Rev. Nucl. Part. Sci. **35**, 295 (1985).

[24] I. I. Strakovsky *et al.*, Yad. Fiz. **40**, 429 (1984) [Sov. J. Nucl. Phys. **40**, 273 (1984)].

[25] M. G. Ryskin and I. I. Strakovsky, Phys. Rev. Lett. **61**, 2384 (1988).

[26] T.-S. H. Lee, Phys. Rev. C **40**, 2911 (1989).

[27] N. Hiroshige *et al.*, Mod. Phys. Lett. **A5**, 207 (1990).

[28] G. M. Shklyarevsky, J. Phys. G **17**, 85 (1991).

[29] N. Hoshizaki, Phys. Rev. C **45**, 1424 (1992); Prog. Theor. Phys. **89**, 245, 251, 563, 569 (1993).

[30] R. Binz *et al.*, Nucl. Phys. **A533**, 601 (1991).

[31] J. M. Fontaine *et al.*, Nucl. Phys. **B358**, 297 (1991).

[32] M. Beddo *et al.*, Phys. Rev. D **50**, 104 (1994); Phys. Lett. **B258**, 24 (1991).

[33] C. Lechanoine-LeLuc and F. Lehar, Rev. Mod. Phys. **65**, 47 (1993), and F. Lehar, private communication.

[34] I. P. Auer *et al.*, Phys. Rev. Lett. **46**, 1177 (1981).

[35] D. P. Grosnick *et al.*, Nucl. Instrum. Methods **A290**, 269 (1990).

[36] J. W. Cronin and O. E. Overseth, Phys. Rev. **129**, 1795 (1963), and references contained in Phys. Rev. D **50**, 1730 (1994).

[37] Ya. S. Derbenev and A. M. Kondratenko, in *Tenth International Conference on High Energy Accelerators*, Protvino, 1977 (IHEP, Protvino, 1977), Vol. II, p. 70; in *High Energy Physics with Polarized Beams and Polarized Targets*, Argonne, 1978, AIP Conf. Proc. No. 51, edited by G. H. Thomas (AIP, New York, 1979), p. 292; Ya. S. Derbenev *et al.*, Particle Accel. **8**, 115 (1978).

[38] D. G. Underwood, Nucl. Instrum. Methods **173**, 351 (1980); in *Eighth International Symposium on High-Energy Spin Physics*, Minneapolis, 1988, AIP Conf. Proc. **187**, edited by K. J. Heller (AIP, New York, 1989), p. 1470.

[39] D. C. Carey *et al.*, Phys. Rev. Lett. **64**, 357 (1990).

[40] H. Primakoff, Phys. Rev. **81**, 899 (1951); A. Halprin, C. M. Andersen, and H. Primakoff, *ibid.* **152**, 1295 (1966).

[41] M. Fukushima *et al.*, Nucl. Phys. B **136**, 189 (1978).

[42] N. Akchurin *et al.*, Phys. Lett. **B229**, 299 (1989); Phys. Rev. D **48**, 3026 (1993); in *Proceedings of the Conference on Intersections Between Particle and Nuclear Physics*, Tucson, 1992, AIP Conf. Proc. **243**, edited by W. T. H. van Oers (AIP, New York, 1992), p. 998.

[43] B. Z. Kopeliovich and L. I. Lapidus, Yad. Fiz. **19**, 218 (1974) [Sov. J. Nucl. Phys. **19**,

114 (1974)]; N. H. Buttimore, E. Gotsman, and E. Leader, Phys. Rev. D **18**, 694 (1978); J. Schwinger, Phys. Rev. **73**, 407 (1948).

[44] P. Chaumette *et al.*, *Advances in Cryogenic Engineering*, vol. 35, edited by R. W. Fast (Plenum, New York, 1990); P. Chaumette *et al.*, in *Ninth International Symposium on High Energy Spin Physics, Workshop on Solid State Polarized Targets*, Bonn, 1990, edited by W. Meyer, E. Steffens, and W. Thiel (Springer-Verlag, Berlin, 1991), Vol. 2, p. 237; P. Chaumette *et al.*, in *Eighth International Symposium on High-Energy Spin Physics*, Minneapolis, 1988, AIP Conf. Proc. **187**, edited by K. J. Heller (AIP, New York, 1989), p. 1331, 1334.

[45] T. O. Niinikoski and F. Udo, Nucl. Instrum. Methods **134**, 219 (1976); T. J. Schmugge and C. D. Jeffries, Phys. Rev. **138**, A1785 (1965); R. Bernard *et al.*, Nucl. Instrum. Methods **176**, 176 (1986).

[46] A. Abragam and M. Goldman, *Nuclear Magnetism: Order and Disorder* (Clarendon, Oxford, 1982).

[47] M. Krumpolc and J. Rocek, J. Am. Chem. Soc. **101**, 3206 (1979).

[48] D. Hill and T. Kasprzyk, Argonne National Laboratory Report No. ANL-HEP-PR-84-32, 1984 (unpublished).

[49] D. Hill, Argonne National Laboratory Report No. ANL-HEP-TR-92-68, 1992 (unpublished).

[50] M. Arignon *et al.*, Nucl. Instrum. Methods **A235**, 523 (1985). The hodoscope described has circular counters, whereas for this experiment rectangular counters are used. The underlying principles of operation and the electronics were identical, however.

[51] K. J. Foley *et al.*, Phys. Rev. Lett. **10**, 376 (1963); **11**, 425, 503 (1963); R. Serber, *ibid.* **13**, 32 (1964).

[52] Y. Watanabe, Phys. Rev. D **19**, 1022 (1979).

[53] E. L. Berger, A. C. Irving, and C. Sorensen, Phys. Rev. D **17**, 2971 (1978); W. Grein and P. Kroll, Nucl. Phys. B **137**, 173 (1978).

[54] G. Ramsey, D. Richards, and D. Sivers, Phys. Rev. D **37**, 3140 (1988); G. Ramsey and D. Sivers, *ibid.* **43**, 2861 (1991).

[55] G. Ramsey, private communication.

[56] D. E. Nagle *et al.*, in *High Energy Physics with Polarized Beams and Polarized Targets*, Argonne, 1978, AIP Conf. Proc. No. 51, edited by G. H. Thomas (AIP, New York, 1979), p. 224; J. M. Potter *et al.*, Phys. Rev. Lett. **33**, 1307 (1974).

[57] N. Lockyer *et al.*, Phys. Rev. D **30**, 860 (1984); Phys. Rev. Lett. **45**, 1821 (1980).

[58] R. W. Harper *et al.*, Phys. Rev. D **31**, 1151 (1985).

[59] V. Yuan *et al.*, Phys. Rev. Lett. **57**, 1680 (1986).

[60] S. Kistryn *et al.*, Phys. Rev. Lett. **58**, 1666 (1987); R. Balzer *et al.*, Phys. Rev. Lett. **44**, 699 (1980).

[61] P. D. Eversheim *et al.*, Phys. Lett. **B256**, 11 (1991).

[62] V. R. Brown, E. M. Henley, and F. R. Krejs, Phys. Rev. Lett. **30**, 770 (1973); Phys. Rev. C **9**, 935 (1974); E. Henley and F. R. Krejs, Phys. Rev. D **11**, 605 (1975).

[63] M. Simonius, Phys. Lett. **41B**, 415 (1972); Nucl. Phys. **A220**, 269 (1974).

[64] Y. Yamamoto, Prog. Theor. Phys. **58**, 1790 (1977).

[65] B. H. J. McKellar and K. R. Lassey, Phys. Rev. C **17**, 842 (1978).

[66] B. Desplanques, J. F. Donoghue, and B. R. Holstein, Ann. Phys. **124**, 449 (1980).

[67] V. B. Kopeliovich and L. I. Frankfurt, Pis'ma Zh. Eksp. Teor. Fiz. **22**, 601 (1975) [JETP

Lett. **22**, 295 (1975)].

[68] T. Oka, Prog. Theor. Phys. **66**, 977 (1981).

[69] A. Barroso and D. Tadić, Nucl. Phys. **A364**, 194 (1981).

[70] D. E. Driscoll and G. A. Miller, Phys. Rev. C **39**, 1951 (1989); **40**, 2159 (1989).

[71] M. J. Iqbal and J. A. Niskanen, Phys. Rev. C **49**, 355 (1994).

[72] L. Kisslinger and G. A. Miller, Phys. Rev. C **27**, 1602 (1983).

[73] L. L. Frankfurt and M. I. Strikman, Phys. Lett. **107B**, 99 (1981).

[74] P. Chiapetta, J. Soffer, and T. T. Wu, J. Phys. G **8**, L93 (1982); J. Soffer, in *High-Energy Physics with Polarized Beams and Targets*, edited by C. Joseph and J. Soffer, Experientia Supplementum Vol. 38 (Birkhäuser Verlag, Basel, 1981), p. 370.

[75] T. Goldman and D. Preston, Nucl. Phys. **B217**, 61 (1983), Phys. Lett. **168B**, 415 (1986).

[76] T. Goldman and D. Preston, in *Proceedings of the Symposium on Future Polarization at Fermilab*, FNAL, 1988, edited by E. Berger *et al.*, (FNAL, 1988), p. 295.

[77] M. Simonius and L. Unger, Phys. Lett. **198B**, 547 (1987).

[78] G. Nardulli and G. Preparata, Phys. Lett. **117B**, 445 (1982); **137B**, 111 (1984).

[79] G. Nardulli, E. Scrimieri, and J. Soffer, Z. Phys. C **16**, 259 (1983).

[80] J. F. Donoghue and B. R. Holstein, Phys. Lett. bf 125B, 445 (1982).

[81] B. H. J. McKellar, Phys. Lett. **138B**, 6 (1984).

[82] B. Desplanques and S. Noguera, Phys. Lett. **144B**, 225 (1984).

[83] L. L. Frankfurt and M. I. Strikman, Phys. Rev. D **33**, 293 (1986).

[84] M. Simonius *et al.*, Nucl. Instrum. Methods **177**, 471 (1980).

FIGURES

FIG. 1. Previous measurements of $\Delta\sigma_L\,(pp)$. Data are taken from Refs. 9–14.

FIG. 2. Diagram of the polarized beam line. Shown in this side view are the production target, Λ decay region, neutral dump, adjustable collimator, beam-tagging region at the intermediate focus, snake magnets, Čerenkov counters, and experimental target. Note the difference in scale between the horizontal and vertical axes.

FIG. 3. Distribution of the number of tagged polarized protons. Those particles tagged with polarization values between -0.35 and -0.55 are assigned negative $(-)$ polarization, $+0.35$ and $+0.55$ positive $(+)$ polarization, and -0.25 and $+0.25$ zero (0) polarization.

FIG. 4. Diagram of the polarized-proton target. Shown in this side view are the dilution refrigerator, target, and polarizing solenoid, which is displayed here in the polarizing position. Particles from the polarized beam entered from the left, were scattered in the target, and exited to the right in this diagram. The solenoid was moved to the left by 16 cm in the frozen spin mode of operation.

FIG. 5. Diagram of the experimental setup. Shown are each of 2 scintillator planes for SNA1, SNA2, and TRA hodoscopes, the snake-magnet apertures, polarized target, and the two veto counters. Also shown is a sample scattering angle, θ, measured by the transmission hodoscope. Not shown in this diagram is the second transmission counter located 46 m downstream of the polarized target. Note the difference in scale between the horizontal and vertical axes.

FIG. 6. Schematic diagram of the $\Delta\sigma_L$ electronic logic.

FIG. 7. Diagram showing the top view of the second "Gray Code" transmission counter. The "direct" counters are shown unshaded and the "inverse" counters are shaded. The second through sixth planes measured the X direction, and the seventh through eleventh measure Y.

FIG. 8. Diagram showing the face of the first transmission counter hodoscope and the algorithm for assigning a t bin for a particle scatter. The grid indicates the segments of the hodoscope and the arcs indicate the t bins calculated for an undeflected trajectory (o) projected to a hodoscope segment. The actual hit (*) in the hodoscope and the calculated ΔX and ΔY positions to assign the appropriate t value are shown.

FIG. 9. Plot of the number of detected counts in the transmission counter as a function of $-t$. The points represent values corrected for geometry, and the dashed line represents a fit to the corrected points.

FIG. 10. Plot of the calculated asymmetry per experimental bin as a function of $-t$. The dashed line is a fit through the data using t-bins 3–11.

FIG. 11. Diagram showing parallel and antiparallel spin states. Each state contains 4 combinations that are composed of the reversible snake, target, and beam-polarization states.

FIG. 12. Plot of the ratio of the number of valid hits in the transmission counter with a proton beam divided by the total number of triggers as a function of the beam polarization.

FIG. 13. Summary of $\Delta\sigma_L$ data from this experiment and corresponding theoretical predictions from Refs. 53–54. The error bars indicate statistical errors only and the extended error bars include both statistical and systematic errors.

FIG. 14. Summary of parity data from previous experiments and this experiment. The three curves indicate theoretical predictions from Ref. 75.

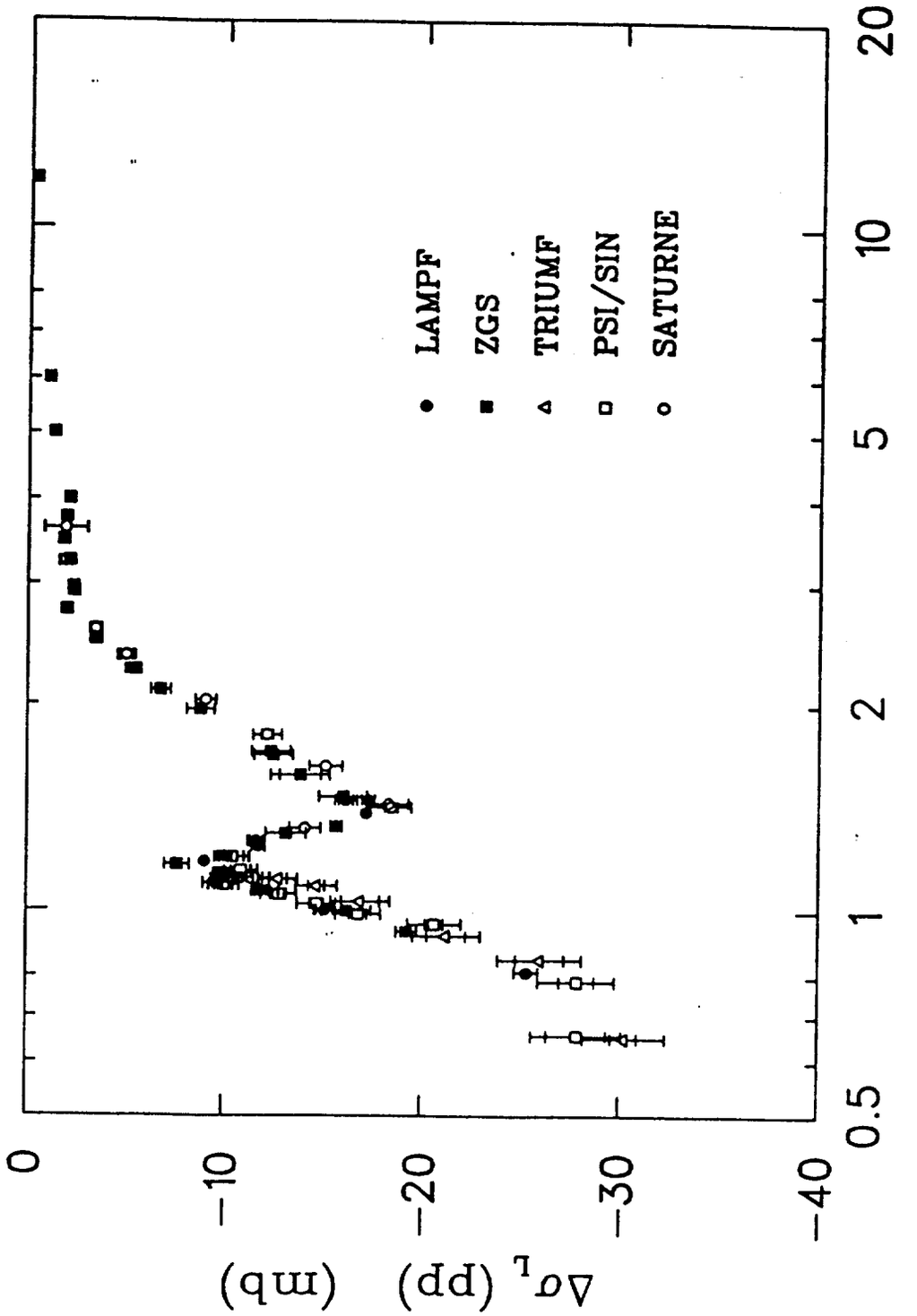
LAMPF
ZGS
TRIUMF
PSI/SIN
SATURNE
$\Delta\sigma_L$ (pp) (mb)
p_{lab} (GeV/c)
0
−10
−20
−30
−40
0.5
1
2
5
10
20

Figure 1

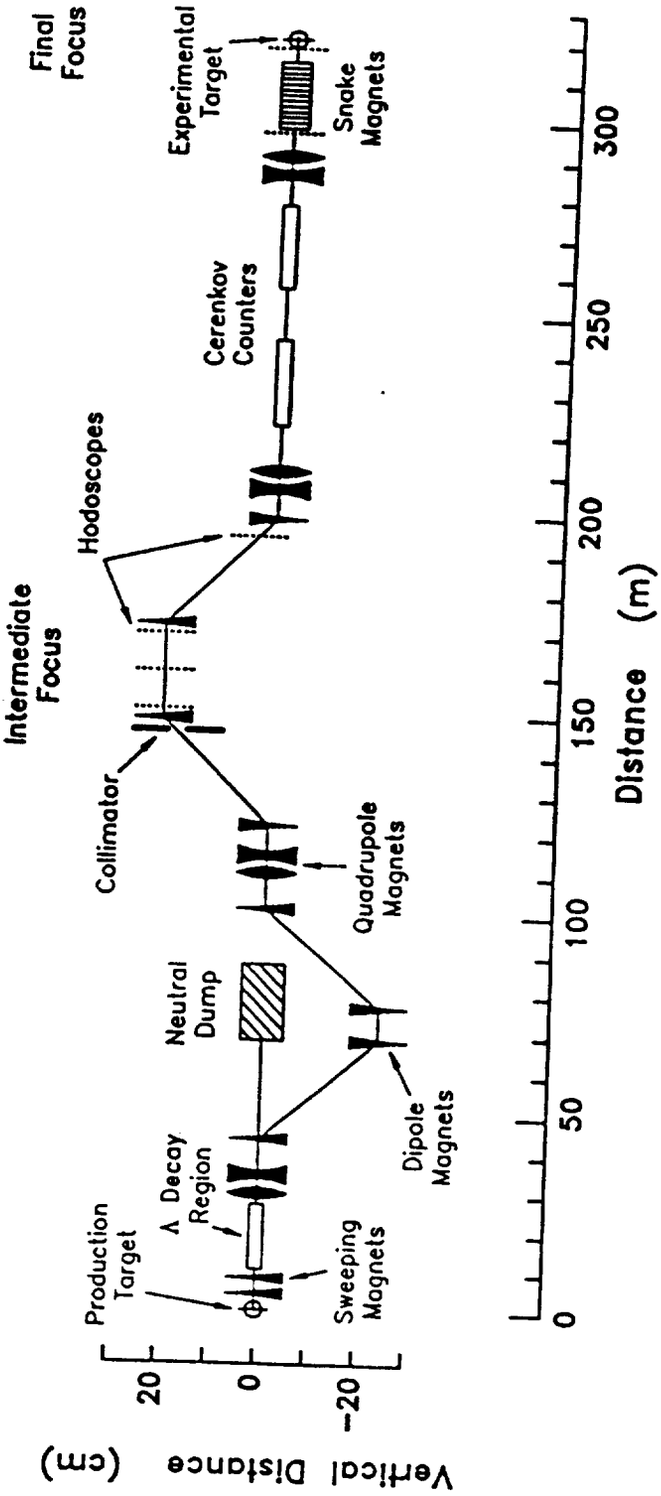
Final Focus
Experimental Target
Snake Magnets
Cerenkov Counters
Hodoscopes
Intermediate Focus
Collimator
Quadrupole Magnets
Neutral Dump
Dipole Magnets
Production Target
Λ Decay Region
Sweeping Magnets
Vertical Distance (cm)
20
0
-20
0
50
100
150
200
250
300
Distance (m)

Figure 2

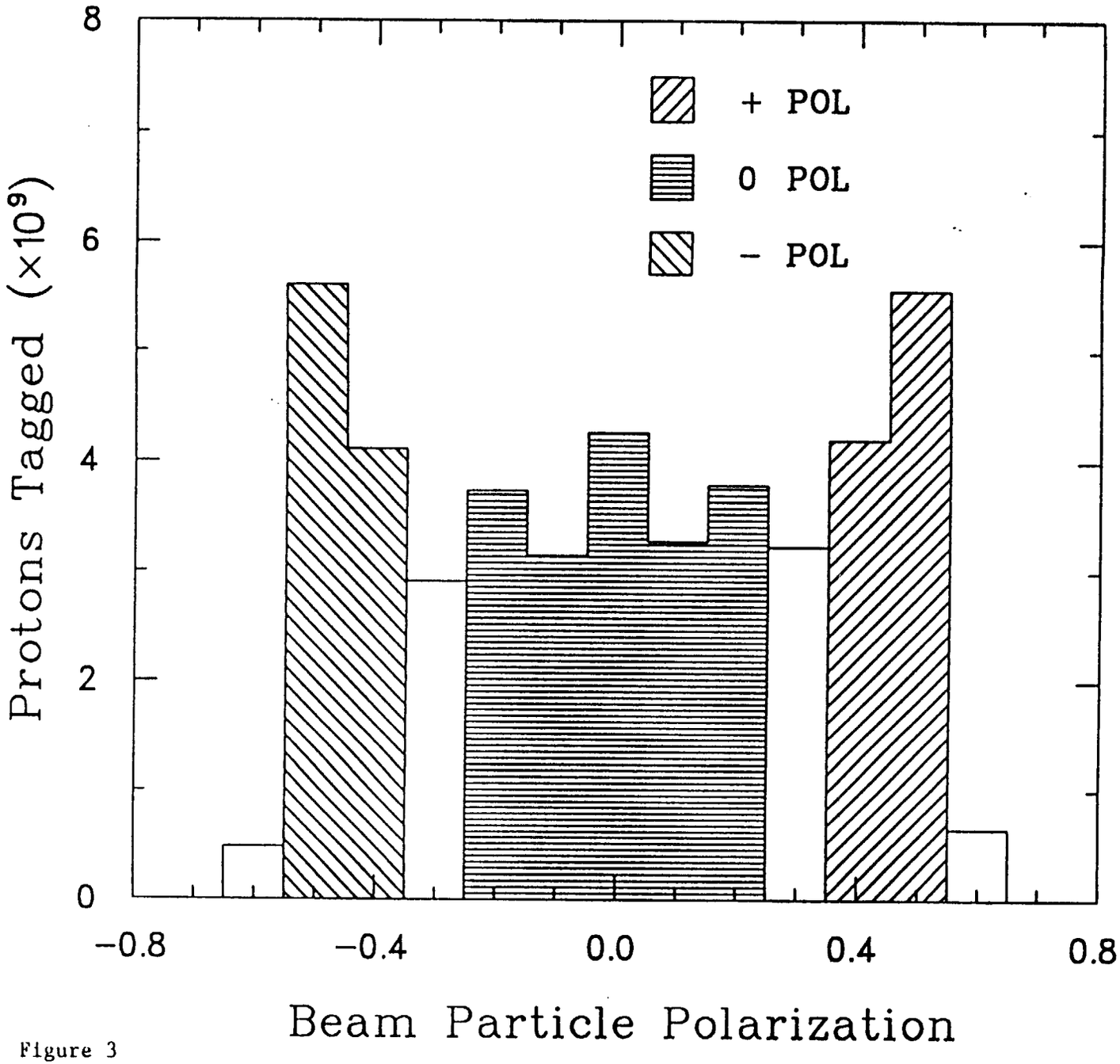
8
6
4
2
0
Protons Tagged (×10⁹)
+ POL
0 POL
− POL
−0.8
−0.4
0.0
0.4
0.8
Beam Particle Polarization

Figure 3

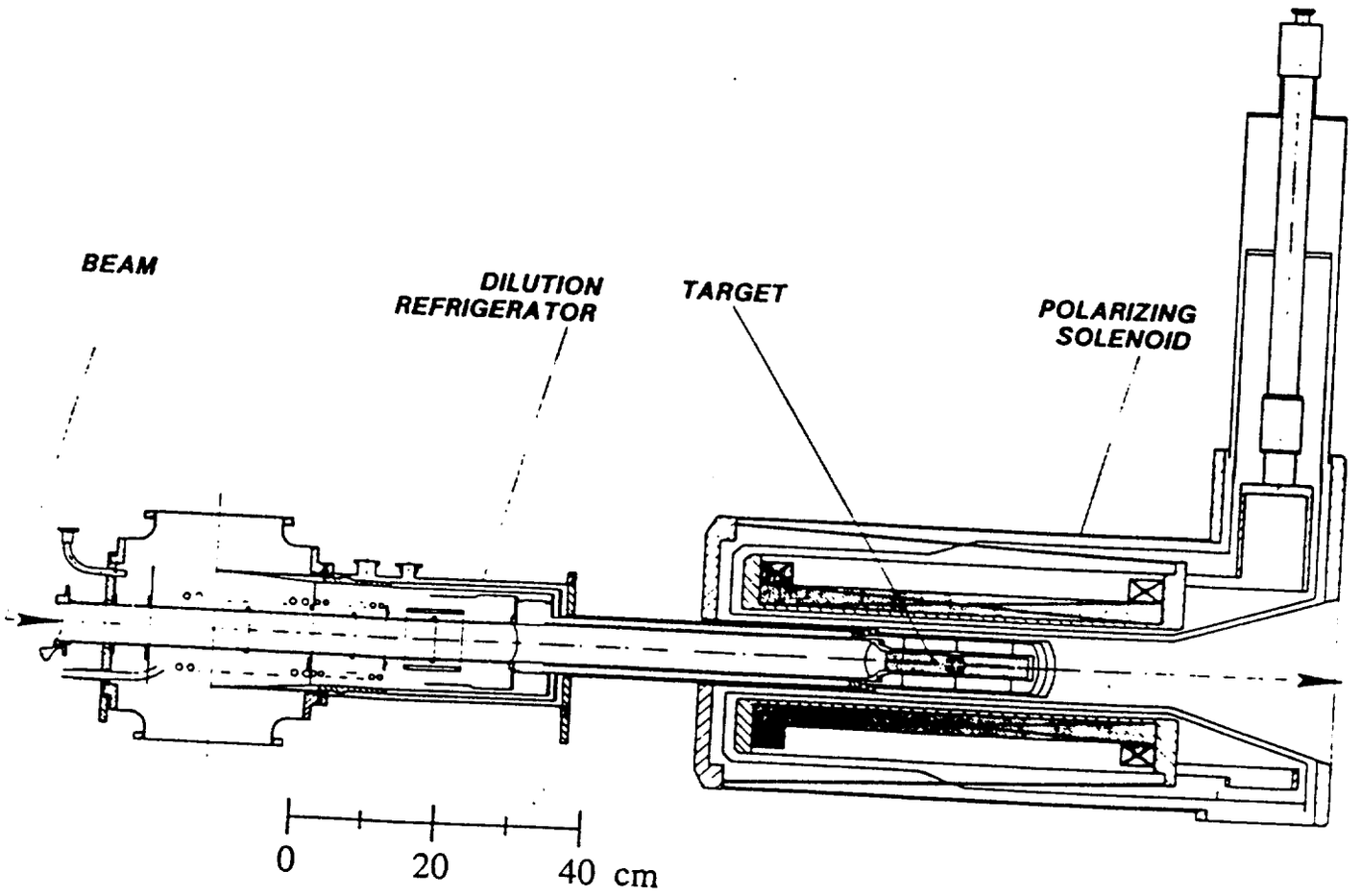
BEAM
DILUTION
REFRIGERATOR
TARGET
POLARIZING
SOLENOID
0
20
40 cm

Figure 4

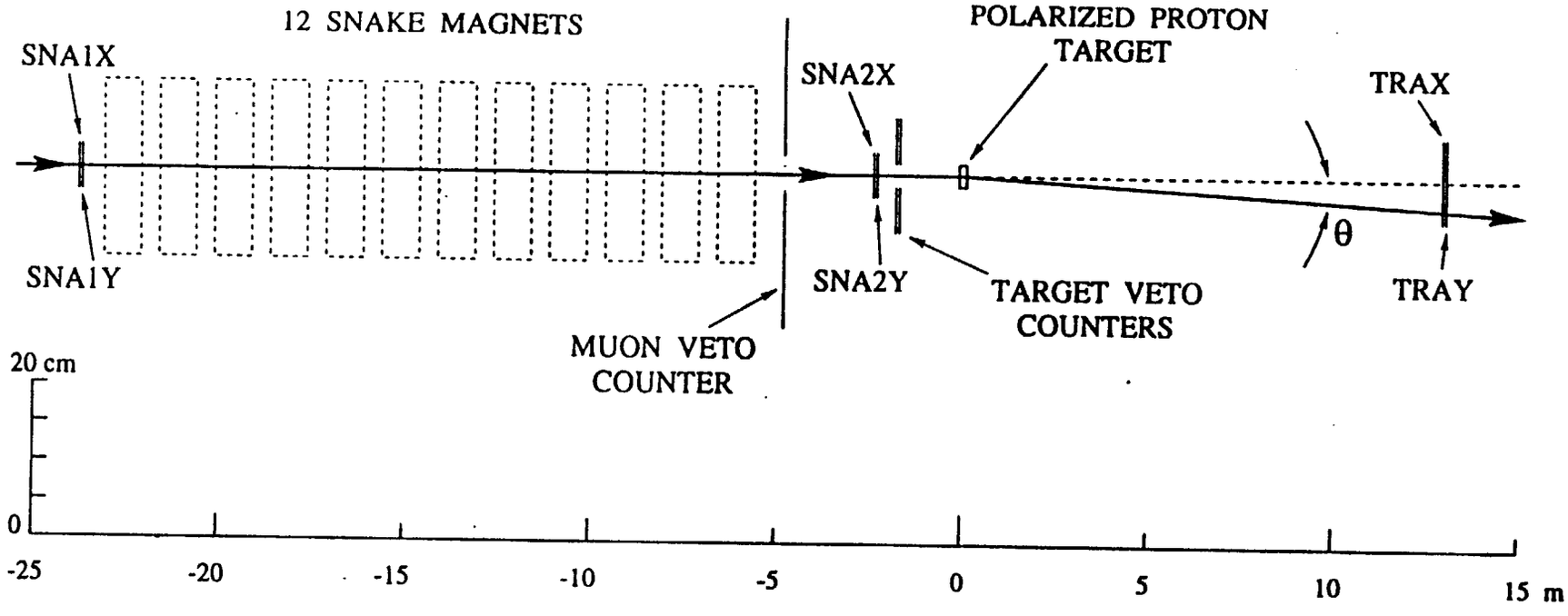
12 SNAKE MAGNETS
SNA1X
SNA1Y
SNA2X
SNA2Y
POLARIZED PROTON TARGET
TRAX
TRAY
θ
TARGET VETO COUNTERS
MUON VETO COUNTER
20 cm
0
-25
-20
-15
-10
-5
0
5
10
15 m

Figure 5

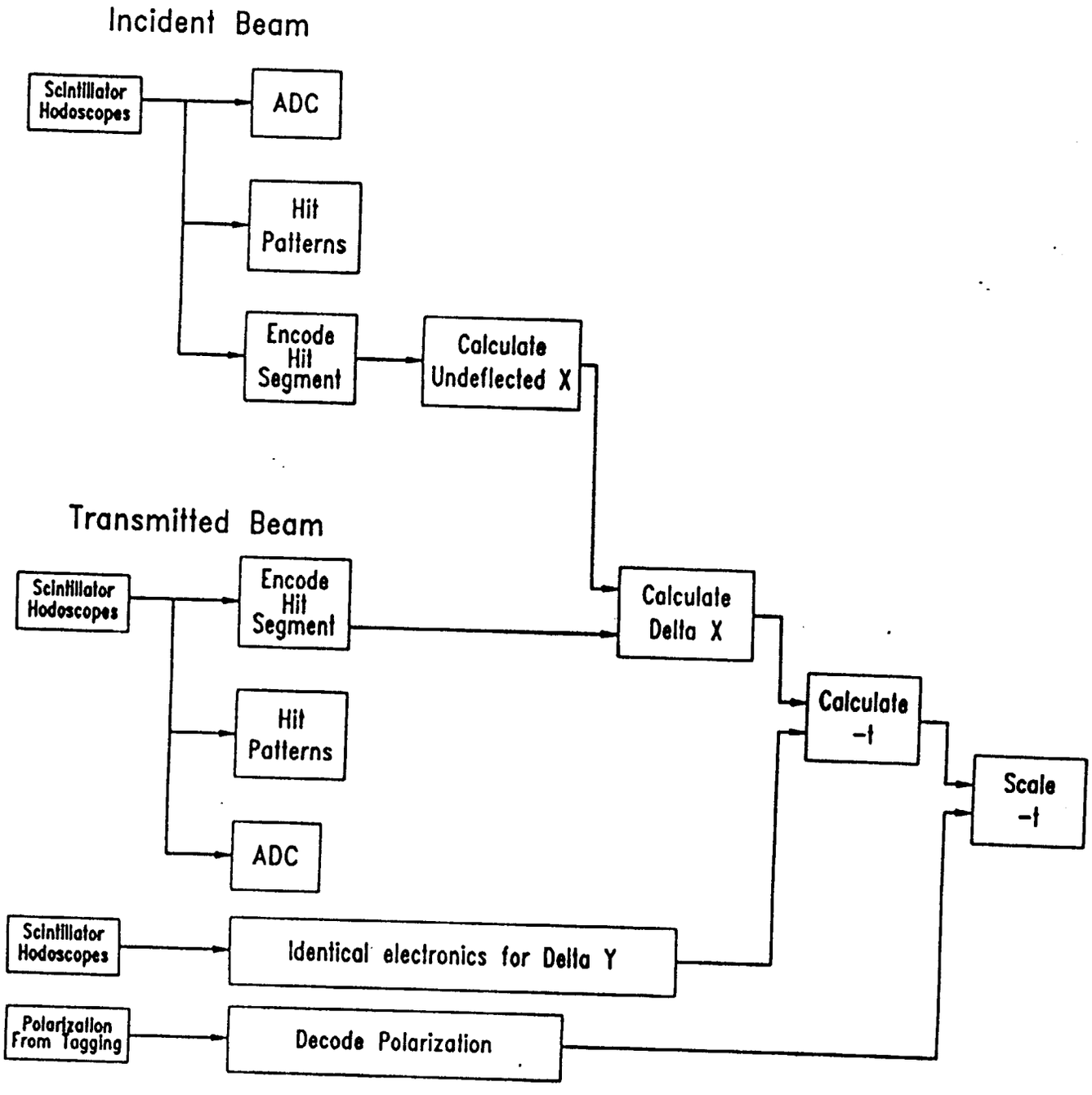
Incident Beam
Scintillator Hodoscopes
ADC
Hit Patterns
Encode Hit Segment
Calculate Undeflected X
Transmitted Beam
Scintillator Hodoscopes
Encode Hit Segment
Calculate Delta X
Calculate -t
Scale -t
Hit Patterns
ADC
Scintillator Hodoscopes
Identical electronics for Delta Y
Polarization From Tagging
Decode Polarization

Figure 6

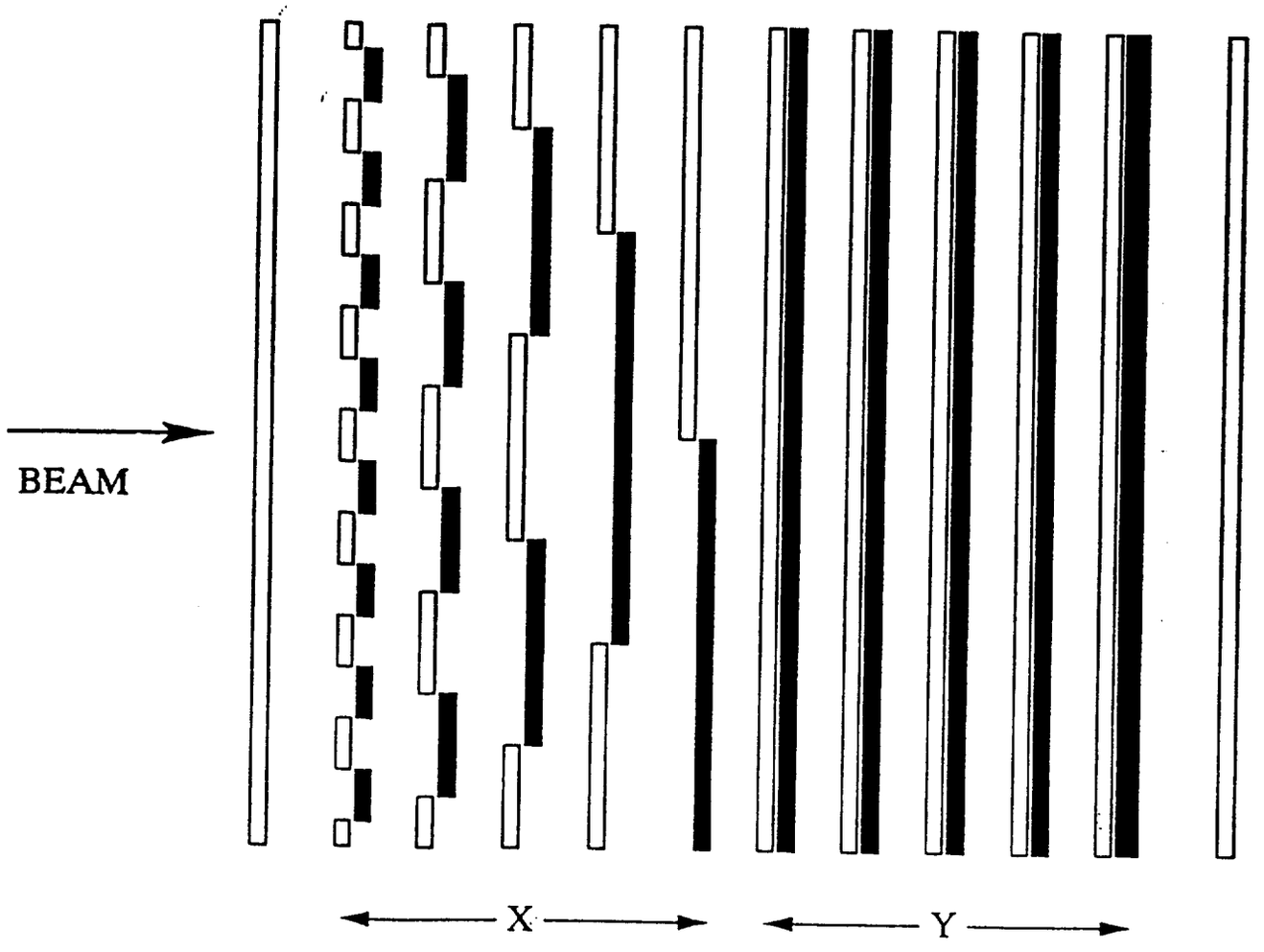

GRAY CODE HODOSCOPE

Figure 7

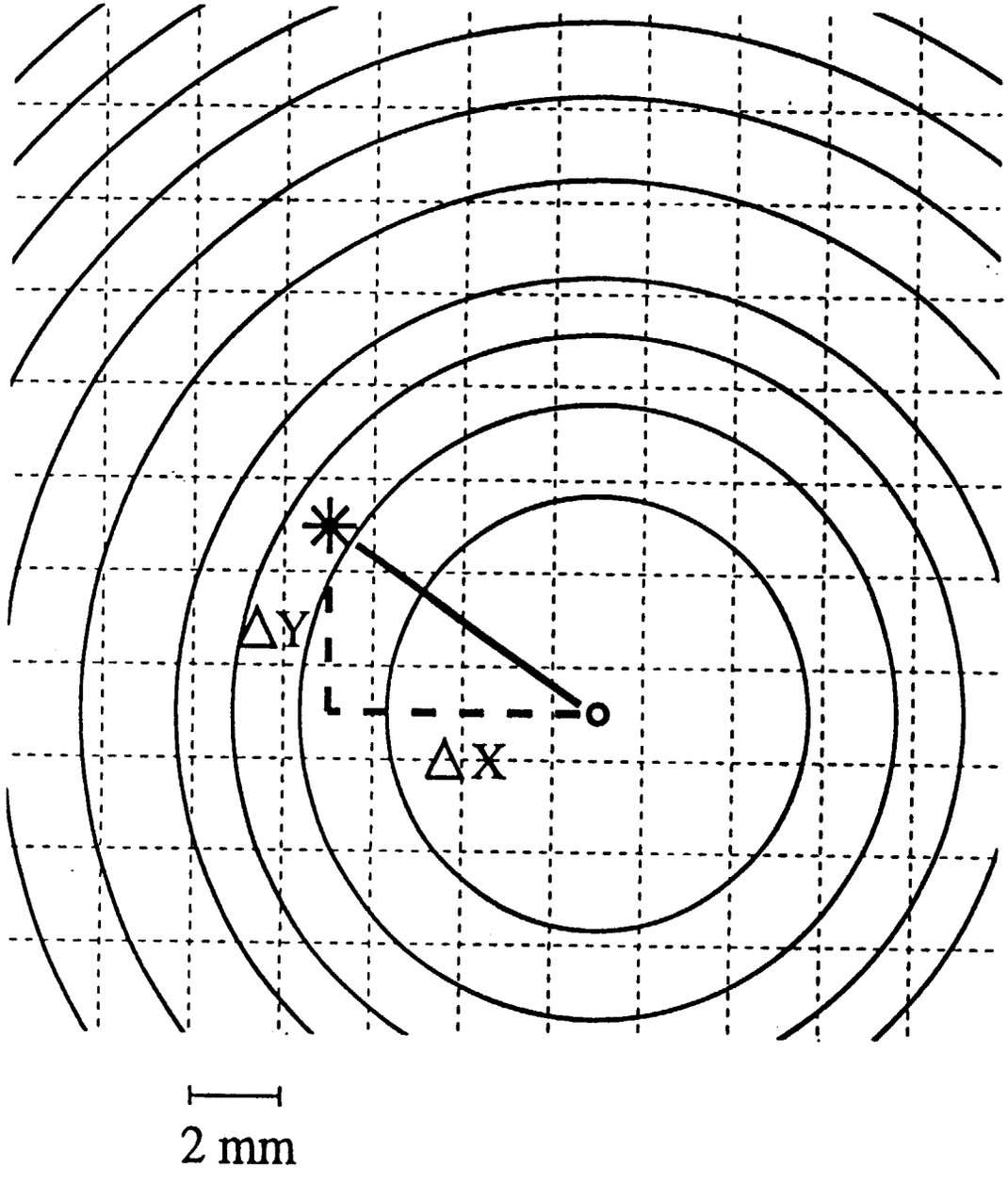

Figure 8

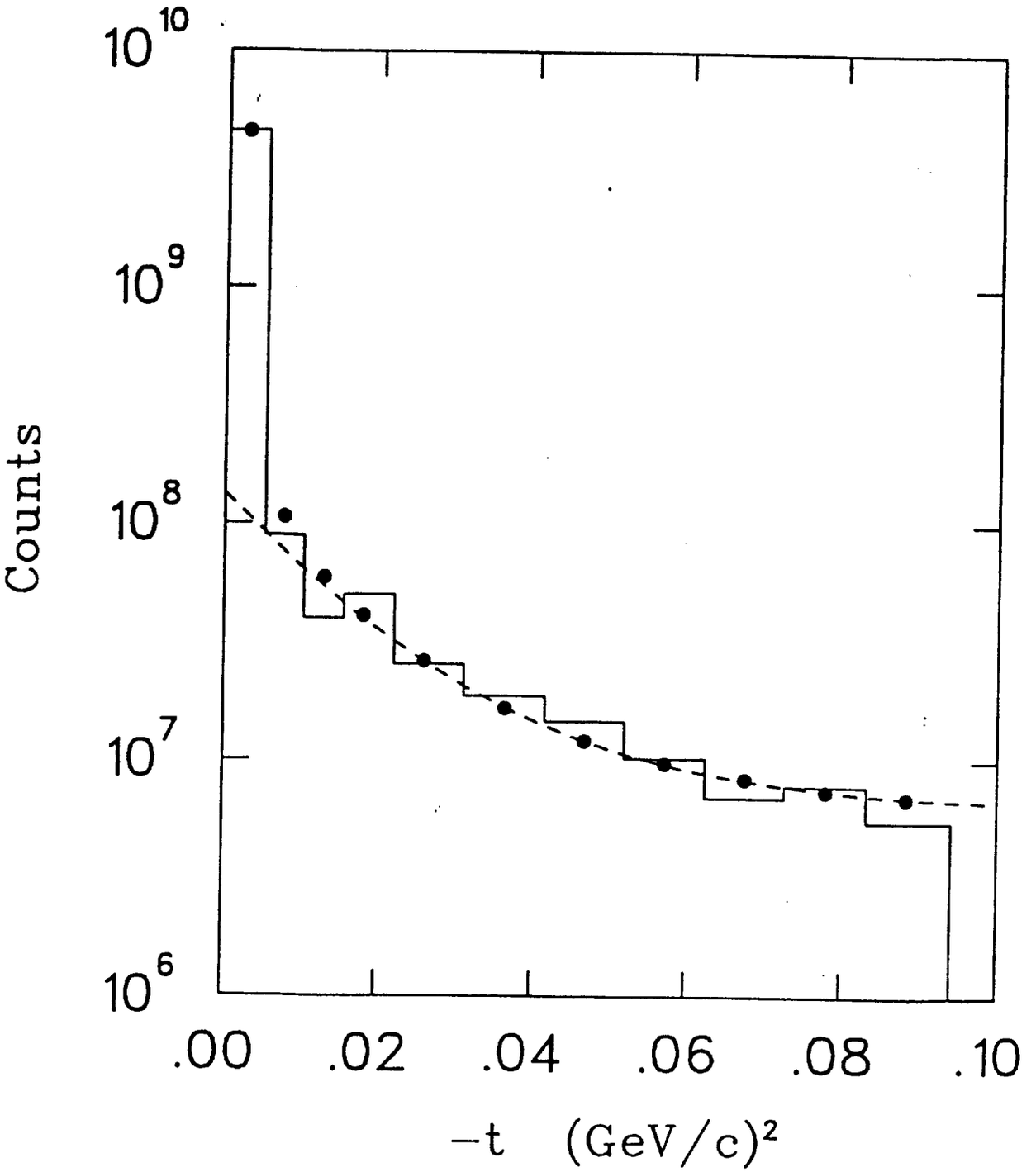

Figure 9

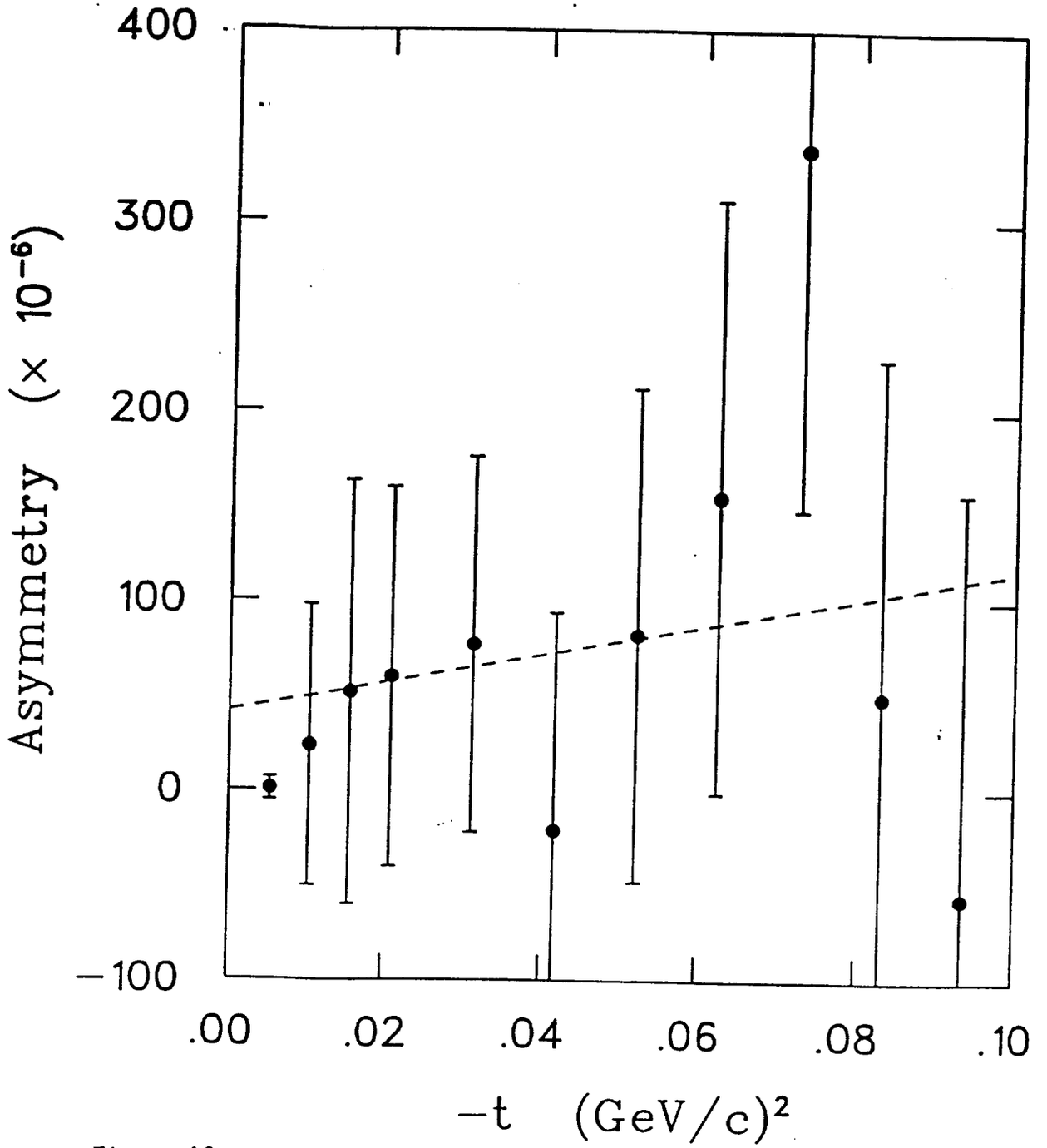

Figure 10

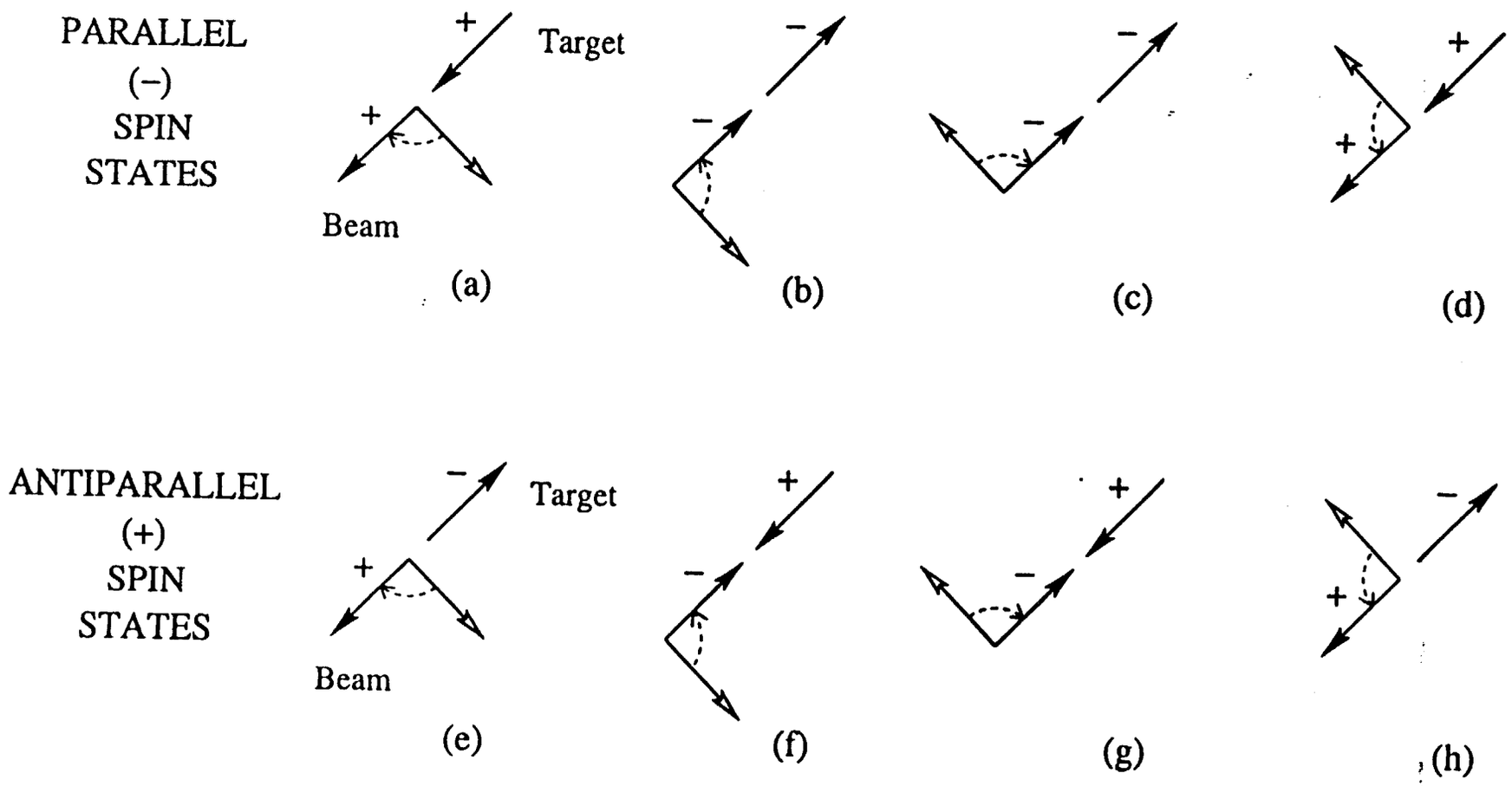
PARALLEL
(−)
SPIN
STATES
+
+
Target
Beam
(a)
−
−
(b)
−
−
(c)
+
+
(d)
ANTIPARALLEL
(+)
SPIN
STATES
−
+
Target
Beam
(e)
+
−
(f)
+
−
(g)
−
+
(h)

Figure 11

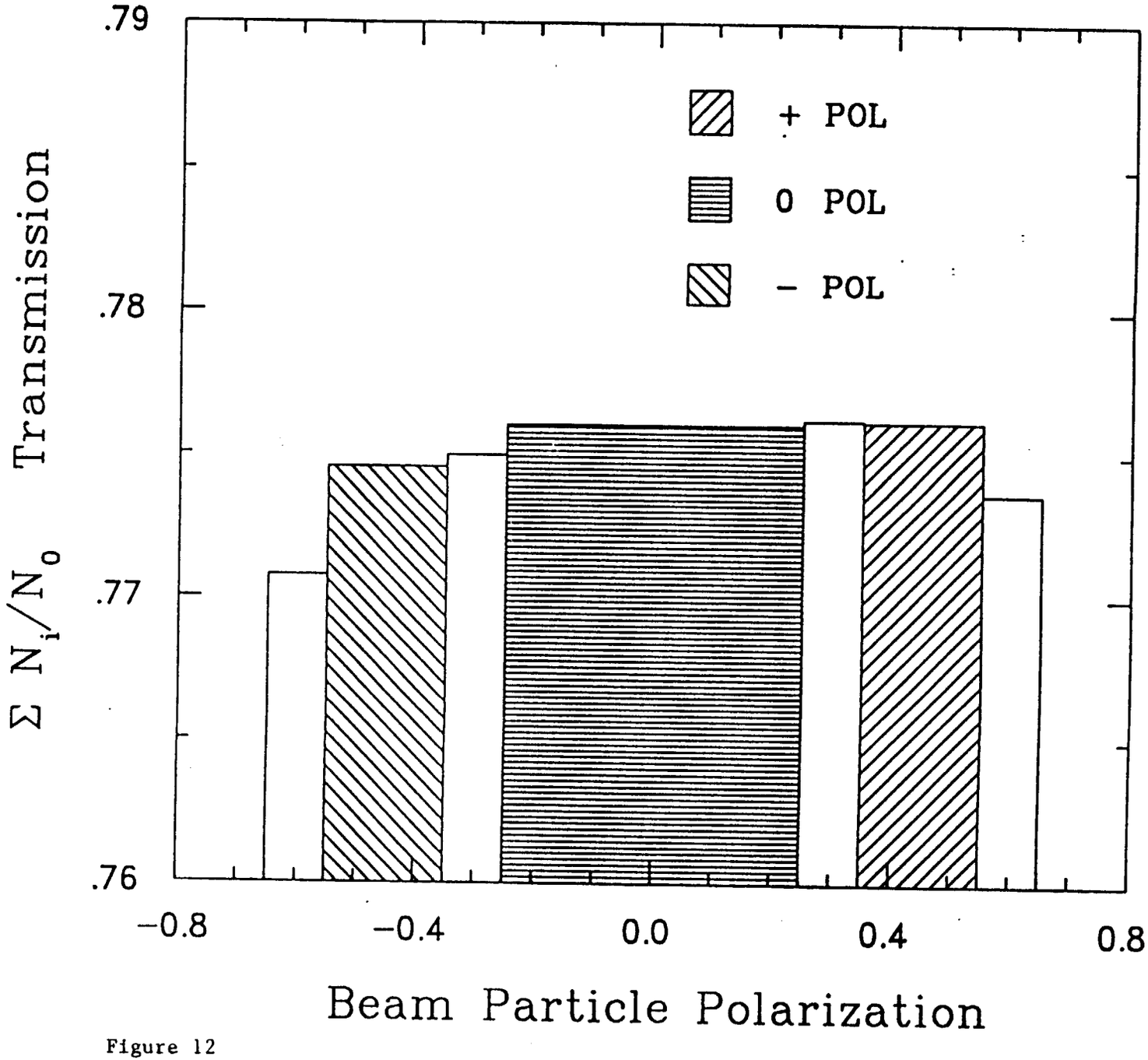
.79
.78
.77
.76
Σ N_i/N_o Transmission
+ POL
0 POL
− POL
−0.8
−0.4
0.0
0.4
0.8
Beam Particle Polarization

Figure 12

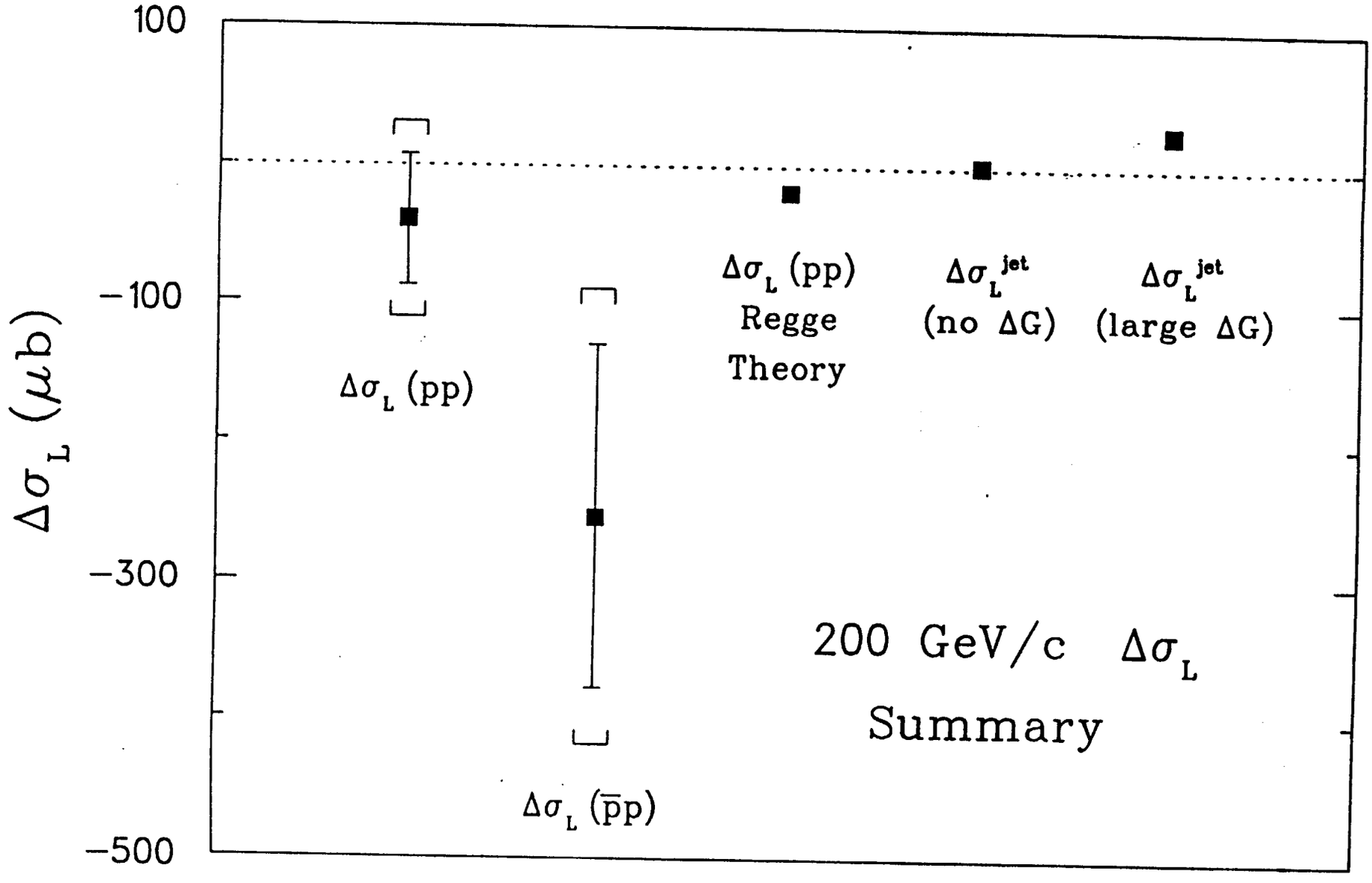
100
−100
−300
−500
$\Delta\sigma_L$ (μb)
$\Delta\sigma_L$ (pp)
$\Delta\sigma_L$ ($\bar{p}p$)
$\Delta\sigma_L$ (pp) Regge Theory
$\Delta\sigma_L^{jet}$ (no ΔG)
$\Delta\sigma_L^{jet}$ (large ΔG)
200 GeV/c $\Delta\sigma_L$
Summary

Figure 13

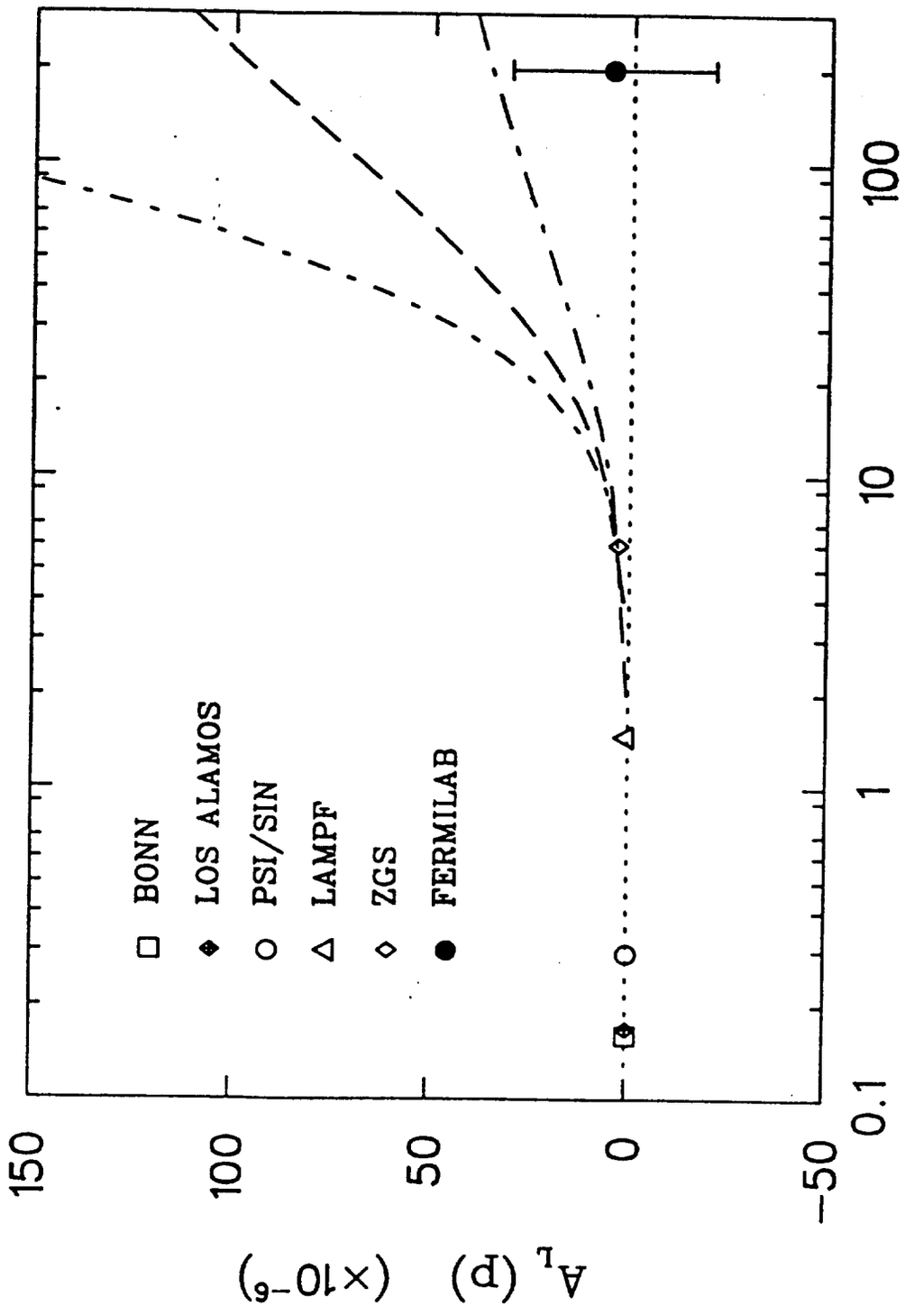
BONN
LOS ALAMOS
PSI/SIN
LAMPF
ZGS
FERMILAB
150
100
50
0
−50
0.1
1
10
100
p_{lab} (GeV/c)
A_L (p) (×10⁻⁶)

Figure 14

TABLES

TABLE I. Table of asymmetries for t bin 1, ϵ_1; background, ϵ_B; and transmission, ϵ; and the uncorrected $\Delta\sigma_L$ value for protons and antiprotons with tagged beam polarization between 0.35–0.55. Errors are statistical only.

Beam	Quantity	Value
p	ϵ_1	$+0.000001 \pm 0.000006$
	ϵ_B	$+0.000042 \pm 0.000084$
	ϵ	$+0.000000 \pm 0.000007$
	$\Delta\sigma_L(pp)$	2 ± 42 μb
$\bar{p}$	ϵ_1	-0.000021 ± 0.000015
	ϵ_B	$+0.000133 \pm 0.000202$
	ϵ	-0.000026 ± 0.000017
	$\Delta\sigma_L(\bar{p}p)$	-150 ± 98 μb

TABLE II. Comparison of results using the two transmission counters and a separate analysis program. $\Delta\sigma_L(I)$ is calculated using data from the first transmission counter, but the global fit method. $\Delta\sigma_L(II)$ is calculated using data from the second transmission counter and the global fit method. These results are not used elsewhere in the paper. The first error shown is statistical and the second is systematic.

Beam	$\Delta\sigma_L(I)$ (μb)	$\Delta\sigma_L(II)$ (μb)
p	$-66 \pm 28 \pm 36$	$-51 \pm 52 \pm 38$
$\bar{p}$	$-68 \pm 87 \pm 82$	$-68 \pm 103 \pm 91$

TABLE III. Table of transmission asymmetries ϵ and $\Delta\sigma_L$ values with a tagged beam polarization of 0.35–0.55 for both protons and antiprotons. The ϵ and $\Delta\sigma_L$ values were analyzed from data for the special conditions listed. The numbers from the special conditions are not used elsewhere in the analysis. Errors are statistical only.

Beam	Quantity	ϵ	$\Delta\sigma_L$ (μb)
p	All data	$+0.000000 \pm 0.000007$	2 ± 42
	+PPT	-0.000045 ± 0.000009	-280 ± 62
	−PPT	$+0.000038 \pm 0.000009$	$+241 \pm 62$
	Snake+	$+0.000018 \pm 0.000009$	$+112 \pm 59$
	Snake−	-0.000018 ± 0.000009	-112 ± 60
	Pol+	-0.000075 ± 0.000009	-469 ± 68
	Pol−	$+0.000044 \pm 0.000009$	$+273 \pm 62$
$\bar{p}$	All data	-0.000026 ± 0.000017	-150 ± 98
	+PPT	-0.000001 ± 0.000024	-7 ± 146
	−PPT	-0.000059 ± 0.000023	-336 ± 134
	Snake+	$+0.000121 \pm 0.000024$	$+708 \pm 148$
	Snake−	-0.000170 ± 0.000024	-997 ± 157

Pol+	$+0.000069 \pm 0.000024$	$+405 \pm 148$
Pol−	-0.000080 ± 0.000023	-469 ± 138

TABLE IV. List of tagged zero beam polarization, ϵ_0; fake zero, ϵ_F; and pairwise spill, ϵ_W, asymmetries for protons and antiprotons. Errors are statistical only.

Beam	ϵ_0	ϵ_F	ϵ_W
p	-0.000064 ± 0.000007	-0.000060 ± 0.000007	-0.000001 ± 0.000006
$\bar{p}$	$+0.000030 \pm 0.000017$	$+0.000073 \pm 0.000017$	-0.000021 ± 0.000015

TABLE V. Calculated left-right, ϵ_{LR}, and up-down, ϵ_{UD}, asymmetries, using the N-type and L-type spin orientation of the proton and antiproton beams. Errors are statistical only.

Orientation	Beam	ϵ_{LR}	ϵ_{UD}
N	p	$+0.002486 \pm 0.000181$	-0.000203 ± 0.000186
	$\tilde{p}$	$+0.001738 \pm 0.000350$	-0.000011 ± 0.000360
L	p	$+0.000179 \pm 0.000036$	-0.000180 ± 0.000037
	$\tilde{p}$	-0.000194 ± 0.000088	$+0.000210 \pm 0.000090$

TABLE VI. Table showing the t dependence of the left- right transmission asymmetry, ϵ_{LR}, using an N-type polarized proton beam. Three ranges of t values are displayed, with the average t value per range also given. Errors are statistical only.

t range	$-t$ $(\mathrm{GeV/c})^2$	ϵ_{LR}
small	0.009	$+0.003875 \pm 0.000335$
mid	0.019	$+0.002616 \pm 0.000300$
large	0.046	$+0.001107 \pm 0.000317$

TABLE VII. List of $\Delta\sigma_L$ transmission, ϵ; fake zero, ϵ_F; fake rotation, ϵ_R; and parity, ϵ_P, asymmetries from target groups for both protons and antiprotons with a tagged beam polarization of 0.35–0.55. Errors are statistical only.

Beam	Group	ϵ ($\times 10^{-6}$)	ϵ_F ($\times 10^{-6}$)	ϵ_R ($\times 10^{-6}$)	ϵ_P ($\times 10^{-6}$)
p	1	146 ± 56	135 ± 56	-2164 ± 56	146 ± 56
	2	-56 ± 20	-107 ± 20	1407 ± 20	56 ± 20
	3	32 ± 17	80 ± 17	-1577 ± 17	32 ± 17
	4	-3 ± 17	-123 ± 17	1473 ± 17	3 ± 17
	5	-154 ± 56	182 ± 56	1697 ± 56	154 ± 56
	6	88 ± 20	-66 ± 20	-1409 ± 20	88 ± 20
	7	-65 ± 25	65 ± 25	1384 ± 25	65 ± 25
	8	91 ± 34	-163 ± 34	-1273 ± 34	91 ± 34
	9	-61 ± 18	83 ± 18	1278 ± 18	61 ± 18
	10	-13 ± 16	-19 ± 16	-1355 ± 16	-13 ± 16
	wt. ave.	-4 ± 7	-15 ± 7	-34 ± 7	41 ± 7
$\bar{p}$	1	-69 ± 40	129 ± 40	1823 ± 40	69 ± 40
	2	-137 ± 44	22 ± 44	-1928 ± 44	-137 ± 44
	3	120 ± 51	95 ± 51	1357 ± 51	-120 ± 51
	4	-1 ± 43	-26 ± 43	-1574 ± 43	-1 ± 43
	5	68 ± 70	103 ± 70	1569 ± 71	-68 ± 70
	6	-94 ± 54	-180 ± 54	-1483 ± 54	-94 ± 54
	7	13 ± 47	166 ± 47	-1563 ± 47	13 ± 47

8	-61 ± 45	-34 ± 45	1506 ± 45	61 ± 45
wt. ave.	-32 ± 17	37 ± 17	-98 ± 17	-24 ± 17

TABLE VIII. List of corrected and uncorrected asymmetries and the total χ^2, the corrections to the asymmetries, and the $\Delta\sigma_L$ value per group for protons with a tagged beam polarization of 0.35–0.55. The total χ^2/d.f. for uncorrected ϵ is 8.0 and for corrected ϵ is 2.2. Errors are statistical only except for the weighted average, where the first error given is statistical and the second is systematic.

Group	Uncorrected ϵ ($\times 10^{-6}$)	χ^2	ϵ_F Correction ($\times 10^{-6}$)	ϵ_R Correction ($\times 10^{-6}$)	Corrected ϵ ($\times 10^{-6}$)	χ^2	$\Delta\sigma_L(pp)$ (μb)
1	146 ± 56	7.2	33 ± 17	-62 ± 10	116 ± 59	4.3	674 ± 345
2	-56 ± 20	6.8	-26 ± 10	41 ± 7	-41 ± 23	2.3	-276 ± 154
3	32 ± 17	4.5	19 ± 7	-45 ± 7	6 ± 20	0.5	37 ± 114
4	-3 ± 17	0.0	-30 ± 10	42 ± 7	10 ± 21	0.7	61 ± 127
5	-154 ± 56	7.2	44 ± 20	49 ± 8	-61 ± 60	0.9	-369 ± 350
6	88 ± 20	21.1	-16 ± 7	-41 ± 7	31 ± 22	3.1	194 ± 135
7	-65 ± 25	6.0	16 ± 8	40 ± 7	-9 ± 27	0.0	-58 ± 157
8	91 ± 34	7.8	-40 ± 15	-37 ± 6	15 ± 38	0.4	95 ± 215
9	-61 ± 18	10.1	20 ± 8	37 ± 6	-4 ± 21	0.1	-32 ± 121
10	-13 ± 16	0.3	-5 ± 4	-39 ± 6	-57 ± 18	8.1	-414 ± 131
wt. ave.	-4 ± 7				-9 ± 8		$-42 \pm 48 \pm 53$

TABLE IX. List of corrected and uncorrected asymmetries and the total χ^2, corrections to the asymmetries, and the $\Delta\sigma_L$ value per group for antiprotons with a tagged beam polarization of 0.35–0.55. The total χ^2/d.f. for uncorrected ϵ is 3.0 and for corrected ϵ is 1.8. Errors are statistical only except for the weighted average, where the first error given is statistical and the second is systematic.

Group	Uncorrected ϵ ($\times 10^{-6}$)	χ^2	ϵ_F Correction ($\times 10^{-6}$)	ϵ_R Correction ($\times 10^{-6}$)	Corrected ϵ ($\times 10^{-6}$)	χ^2	$\Delta\sigma_L(\bar{p}p)$ (μb)
1	-69 ± 40	0.9	-66 ± 33	-24 ± 19	-159 ± 55	4.5	-983 ± 344
2	-137 ± 44	5.8	-11 ± 23	26 ± 20	-123 ± 53	2.0	-688 ± 302
3	120 ± 51	8.8	-49 ± 32	-18 ± 14	53 ± 62	2.4	307 ± 361
4	-1 ± 43	0.5	13 ± 23	21 ± 16	33 ± 51	2.3	198 ± 297
5	68 ± 70	2.0	-53 ± 41	-21 ± 16	-6 ± 83	0.2	-38 ± 504
6	-94 ± 54	1.4	92 ± 45	20 ± 15	18 ± 72	0.8	111 ± 419
7	13 ± 47	0.9	-85 ± 41	21 ± 16	-51 ± 64	0.0	-295 ± 361
8	-61 ± 45	0.4	17 ± 24	-20 ± 15	-64 ± 53	0.2	-388 ± 327
wt. ave.	-32 ± 17				-45 ± 21		$-256 \pm 124 \pm 109$

TABLE X. Parity data for protons with a tagged beam polarisation of 0.35-0.55. Listed are the uncorrected and corrected asymmetries, ϵ_P, the total χ^2, and the A_L value per group. The uncorrected χ^2/d.f. is 8.0 and the corrected value is 2.4. Errors are statistical only except for the weighted average, where the first error is statistical and the second is systematic.

Group	Uncorrected ϵ_P ($\times 10^{-6}$)	Corrected ϵ_P ($\times 10^{-6}$)	χ^2	A_L ($\times 10^{-6}$)
1	146 ± 56	116 ± 59	3.7	254 ± 129
2	56 ± 20	41 ± 23	2.9	89 ± 49
3	32 ± 17	6 ± 20	0.0	14 ± 43
4	3 ± 17	-10 ± 21	0.4	-22 ± 45
5	154 ± 56	61 ± 60	1.0	138 ± 131
6	88 ± 20	31 ± 22	1.8	70 ± 48
7	65 ± 25	9 ± 27	0.1	22 ± 59
8	91 ± 34	15 ± 38	0.1	36 ± 81
9	61 ± 18	4 ± 21	0.0	12 ± 44
10	-13 ± 16	-57 ± 18	11.5	-123 ± 38
wt. ave.	41 ± 7	2 ± 8		$5 \pm 17 \pm 20$

TABLE XI. Parity data for antiprotons with a tagged beam polarisation of 0.35–0.55. Listed are the uncorrected and corrected asymmetries, ϵ_P, and the total χ^2, and the A_L value per group. The uncorrected χ^2/d.f. is 3.0 and the corrected value is 2.4. Errors are statistical only except for the weighted average, where the first error is statistical and the second is systematic.

Group	Uncorrected ϵ_P ($\times 10^{-6}$)	Corrected ϵ_P ($\times 10^{-6}$)	χ^2	A_L ($\times 10^{-6}$)
1	69 ± 40	159 ± 55	7.5	351 ± 120
2	-137 ± 44	-123 ± 53	6.3	-269 ± 116
3	-120 ± 51	-53 ± 62	1.0	-115 ± 135
4	-1 ± 43	33 ± 51	0.2	74 ± 112
5	-68 ± 70	6 ± 83	0.0	14 ± 187
6	-94 ± 54	18 ± 72	0.0	42 ± 158
7	13 ± 47	-51 ± 64	1.0	-114 ± 139
8	61 ± 45	64 ± 53	1.0	139 ± 117
wt. ave.	-24 ± 17	10 ± 21		$22 \pm 46 \pm 55$